Reconstruction of Ablative Thermal Protection System Aeroheating Using a Green's Function Approach

Kenneth McAfee* and Oded Rabin†
University of Maryland, College Park, Maryland 20742
and
Hannah S. Alpert‡
NASA Ames Research Center, Moffett Field, California 94035

https://doi.org/10.2514/1.A36673

Reconstructing the heating conditions experienced by spacecraft during atmospheric entry often requires the use of inverse heat transfer (IHT) techniques. Current IHT techniques, however, demand substantial computational resources and are impractical for analyses such as uncertainty quantification and real-time health monitoring. In this work, a Green's function IHT approach is developed to efficiently recover atmospheric entry heating conditions from thermal protection system (TPS)-embedded temperature probe measurements. A multiparameter Cole–Hopf transformation is proposed to render the heat conduction equation for pyrolyzing solids compatible with the Green's function formalism. The algorithm is validated using arc-jet test data and is used to reconstruct the atmospheric entry heating conditions on the Mars 2020 backshell. The performance of the algorithm is benchmarked against the state-of-the-art IHT framework FIAT_Opt. Notably, the approach recovers the incident heat flux from the aeroheating environment to within 6% of FIAT_Opt in over two orders of magnitude less time. The efficiency of the algorithm is leveraged to compute the uncertainty contributions of input parameters to the total uncertainty of the reconstructed Mars 2020 backshell heating conditions. The sensitivity analysis uncovers that uncertainties in the TPS specific heat, thermal conductivity, and emissivity are dominant drivers of the reconstruction uncertainty at different times during atmospheric entry.

Nomenclature

A	=	Cole–Hopf transformation constant
C_H	=	film coefficient, $\mathrm{kg/(m^2 \cdot s)}$
C_p	=	specific heat, $\mathrm{J/(kg \cdot K)}$
e	=	specific internal energy, J/kg
f_1, f_2	=	Cole–Hopf transformation functions
$\hat{f}$	=	Galerkin basis functions
G	=	Green's function, 1/m
$g(x,t)$	=	internal source term, $\mathrm{W/m^3}$
h	=	specific enthalpy, J/kg
k	=	thermal conductivity, $\mathrm{W/(m \cdot K)}$
L	=	thickness, m
$\dot{m}$	=	mass flux, $\mathrm{kg/(m^2 \cdot s)}$
N	=	basis function order
N_t	=	number of measurement sample points
N_x	=	number of integration points for numerical quadrature
q	=	heat flux, $\mathrm{W/m^2}$
T	=	temperature relative to initial conditions or a reference temperature, K
$\tilde{T}$	=	absolute temperature, K
$\tilde{T}_s$	=	absolute surface temperature, K
t	=	time, s
x	=	position coordinate, m
x_0	=	dummy position coordinate, m
α	=	thermal diffusivity, $\mathrm{m^2/s}$
β	=	Cole–Hopf transformation parameter
ϵ	=	emissivity
θ	=	transformed temperature
$\Lambda_{n,n}$	=	eigenvalues
μ	=	mean
ξ	=	transformed position coordinate
ρ	=	density, $\mathrm{kg/m^3}$
σ	=	standard deviation
σ_{SB}	=	Stefan–Boltzmann constant, $\mathrm{W/(m^2 \cdot K^4)}$
τ	=	dummy time variable, s
ϕ	=	porosity
ϕ_n	=	eigenfunctions
χ	=	char volume fraction
ψ_n	=	eigenvectors

Subscripts

ad	=	adhesive
c	=	char
conv	=	convective
g	=	pyrolysis gas
HW	=	hot-wall
inc	=	incident
rad	=	radiative
sub	=	substructure
TPS	=	Thermal Protection System
v	=	virgin
0	=	initial or reference condition

Portions of this work presented as Paper 2025-2704 at the 2025 AIAA SciTech Forum, Orlando, FL, January 6–10, 2025; received 16 December 2025; accepted for publication 20 April 2026; published online Open Access 7 July 2026.

*Graduate Student, Department of Aerospace Engineering; kenneth.s.mcafee@nasa.gov (Corresponding Author).

†Associate Professor, Department of Materials Science and Engineering, Institute for Research in Electronics and Applied Physics; oded@umd.edu (Co-Corresponding Author).

‡Systems Engineer, Entry Systems and Vehicle Development Branch.

I. Introduction

RECONSTRUCTIONS of the heat loads experienced by atmospheric entry spacecraft are critical to validate computational models, evaluate the performance of thermal protection systems (TPS), and probe high-speed aerothermodynamic phenomena. To this end, recent space exploration missions have featured extensive thermal instrumentation suites embedded in the TPS, including direct heat flux sensors, radiometers, thermocouple plugs with one or more temperature probes embedded at various depths, and discrete temperature sensors [1–3]. Most commonly, postflight analyses of atmospheric entry heating have leveraged subsurface temperature probe measurements within inverse heat transfer (IHT) methods, where the surface heat flux boundary condition is recovered using the measured in-depth temperature time history and the known material properties of the TPS [4]. While often numerically complex, IHT methods are essential to recover the heating conditions that best represent those experienced by the TPS, which may be strongly influenced by contributions from radiative emission, convection from subsurface decomposition products, or gas–surface interactions with the boundary layer [5]; critically, these contributions are not captured by measurements from direct heat flux sensors [6], which often must be passively cooled due to stringent design limitations [3]. IHT methods are also applicable to a wider range of space exploration missions due to the more pervasive use of temperature sensors embedded in TPS and can be implemented retroactively to analyze atmospheric entry heating for any space exploration mission that featured in-depth temperature measurements [7]. Furthermore, IHT methods can be utilized in ground testing applications to characterize the heating conditions on a test article whose surface is neither in an adiabatic nor an isothermal state and cannot be inferred directly from reference cold-wall calorimeter measurements [8]. These advantages, by and large, motivate the development of IHT techniques purpose-built for the reconstruction of atmospheric entry aeroheating.

Current IHT methods used to reconstruct the heating conditions on spacecraft during atmospheric entry typically rely on high-fidelity multiphysics simulations embedded within a nonlinear objective function minimization framework. The two most prevalent algorithms used by the atmospheric entry community are FIAT_Opt [4] and INHEAT [5,9]. FIAT_Opt leverages the Fully Implicit Ablation and Thermal Analysis program (FIAT) [10], developed at NASA Ames, within a Gauss–Newton or Levenberg–Marquardt optimization routine. INHEAT leverages the CHarring Ablator Response code (CHAR) [11], developed at NASA Johnson, embedded in an adaptation of the function specification method [12]. Both approaches have been developed in the past 12 years, either within the scope of the Artemis program (INHEAT) or for interplanetary space exploration (FIAT_Opt). Notably, FIAT_Opt (and its underlying methodology [13]) has been used to reconstruct the heat loads on the Mars 2020 [4] and Mars Science Laboratory [14] atmospheric entry spacecraft.

Both IHT methods, however, demand substantial computational resources. This cost is rooted in the complex material response behavior of ablative TPS, which drives the use of well-established multiphysics codes, such as FIAT and CHAR, in the IHT formulation. These codes employ a spatially discretized mesh and implicit time-marching finite volume or finite element schemes, which increase the computational overhead of the IHT problem in two ways: I) although the objective function to be minimized only considers the thermal response at the temperature measurement location, the whole-domain solution is required at each time step, and II) the solution must be calculated using iterative nonlinear optimization routines, which require the evaluation of local objective function gradients—i.e., the change in the objective function with respect to change in the surface heat flux boundary condition—for each iteration [5]. The main implication of the latter is that, for nonlinear material systems, many (>1000) individual simulations may be needed to converge on a single heat flux solution [4]. Generally, these drawbacks persist in all iterative IHT algorithms that rely on mesh discretization and time-marching schemes [15–17] but are exacerbated in approaches tailored for ablative TPS materials due to the comparatively large cost of single solution evaluations.

The Green's function approach offers a computationally efficient framework well-suited to address the drawbacks associated with current IHT methods for atmospheric entry applications. In contrast to the prevailing time-marching IHT methods [4,5], the mesh-free Green's function approach models the material response only at a single location (i.e., the temperature measurement location) but for the entire time series at once [18]. Green's function-based approaches, thus, often require substantially less computational overhead than other IHT methods. Green's functions have been leveraged extensively in the aerothermodynamics community to efficiently model heat conduction phenomena in ground test articles to probe boundary-layer phenomena, with prior art including algorithms that can accommodate multilayered structures [19] and nonlinear temperature measurement phenomena [20]. Critically, recent adaptations of the Green's function formulation to material systems with temperature-dependent thermal properties have demonstrated that the approach can be applied to more complex IHT problems [19,21], with amenability for the class of ablative materials used on entry spacecraft.

In this work, a Green's function IHT approach is developed to reconstruct the heat loads experienced by spacecraft during atmospheric entry. The Green's function formalism is adapted to model the effects of nonlinear heat conduction phenomena in ablative TPS materials, such as pyrolysis and internal gas transport, for accurate reconstruction of the surface heating conditions. The approach is verified using open-source material response codes and validated using measurements from the Panel Arc-Jet Test Facility (PTF) at NASA Ames. The algorithm is then used to reconstruct the heating conditions on the Mars 2020 backshell during atmospheric entry and characterize the reconstruction uncertainty contributions from model system input parameters via a full-flight variance-based sensitivity analysis.

II. Reconstruction Algorithm

The objective of the reconstruction algorithm is to recover the TPS surface heating conditions using the temperature time history from a probe embedded in the TPS. The approach consists of three steps. First, a Green's function formulation is developed to efficiently model the transient heat conduction within the TPS at the temperature measurement location. Due to the strong temperature and composition dependence of the thermophysical properties of pyrolyzing TPS materials, the governing heat conduction equation is pretreated with a multiparameter Cole–Hopf transform to render it compatible with the Green's function formalism. In the second step, the Green's function representation of the TPS thermal history is inverted to recover the net hot-wall heat flux absorbed at the TPS surface. In the third step, the reconstructed net hot-wall heat flux is used to calculate the TPS surface temperature and char state to predict the heat flux solely from the external aeroheating environment.

The reconstruction algorithm is developed for the multimaterial one-dimensional (1D) model system shown in Fig. 1. The model system is representative of common TPS stack-up configurations flown on entry spacecraft and consists of an ablative TPS, an adhesive layer, and a substructure with thicknesses of L, L_{ad}, and L_{sub}, respectively. The adhesive and substructure domains do not decompose and are modeled using constant thermal properties. The origin of the coordinate system ($x = 0$) is set at the interface between the TPS and the adhesive. The temperature probe is embedded in the TPS at a depth of $L - x_T$. The external surface of the TPS is exposed to the aeroheating environment, which results in a net hot-wall heat flux q_{HW} conducted into the solid. The internal surface of the stack-up is modeled as insulating.

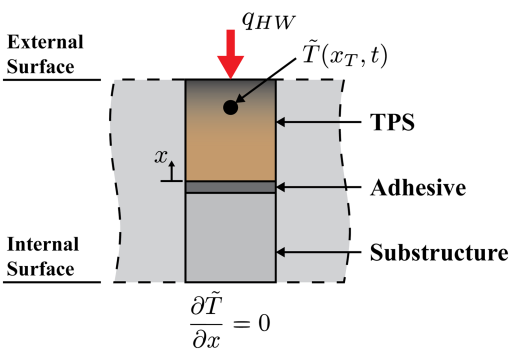

Fig. 1 One-dimensional model system schematic. The temperature measurement is sampled from a probe embedded in the TPS at x_T.

A. Green's Function Formulation for Ablative TPS

1. Heat Conduction in Pyrolyzing Solids

The temperature distribution within the TPS solid is governed by the heat conduction equation:

$$\rho_s C_p(\tilde{T},\chi)\frac{\partial \tilde{T}}{\partial t} - \frac{\partial}{\partial x}\left[k(\tilde{T},\chi)\frac{\partial \tilde{T}}{\partial x}\right] = g(x,t) \tag{1}$$

In Eq. (1), ρ_s, C_p, and k represent the TPS material density, specific heat, and thermal conductivity, respectively. The parameter $\tilde{T}$ represents the absolute temperature, and χ represents the char volume fraction, defined as a function of density:

$$\chi = \frac{\rho_s - \rho_v}{\rho_c - \rho_v} \tag{2}$$

where the subscripts v and c correspond to fully virgin and fully charred material properties, respectively. Effective thermophysical properties are interpolated between virgin and char states, as per [11]

$$C_p(\tilde{T},\chi) = (1-\chi)\frac{\rho_v}{\rho_s}C_{p,v}(\tilde{T}) + \chi\frac{\rho_c}{\rho_s}C_{p,c}(\tilde{T}) \tag{3}$$

$$k(\tilde{T},\chi) = (1-\chi)\frac{\rho_v}{\rho_s}k_v(\tilde{T}) + \chi\frac{\rho_c}{\rho_s}k_c(\tilde{T}) \tag{4}$$

The inhomogeneous source term on the right-hand side of Eq. (1) is included to capture the effects of volumetric energy generation phenomena, such as decomposition and internal convection. Adapted from [22,10],

$$g(x,t) = \left(h_g - \frac{\rho_c h_c - \rho_v h_v}{\rho_c - \rho_v}\right)\frac{\partial \rho_s}{\partial t} - \frac{\partial}{\partial t}(\phi \rho_g e_g) - \dot{m}_g\frac{\partial h_g}{\partial x} \tag{5}$$

The first term on the right-hand side of Eq. (5) represents the net rate of enthalpy change as the virgin TPS decomposes into a mixture of solid char and pyrolysis gas, where h_g, h_v, and h_c represent the specific enthalpy of the pyrolysis gas, fully virgin solid, and fully charred solid, respectively. The solid decomposition rate $\partial\rho_s/\partial t$ is modeled using a set of Arrhenius rate equations as per [22,10], detailed in the Appendix. The second term on the right-hand side of Eq. (5) captures the rate of change of the internal energy of the pyrolysis gas e_g, where ϕ represents the porosity of the solid. The third term on the right-hand side of Eq. (5) accounts for the effects of pyrolysis gas convection, where $\dot{m}_g$ is the mass flux of the pyrolysis gas toward the TPS surface. The pyrolysis gas mass flux is approximated by considering mass conservation of the gas phase:

$$\frac{\partial \rho_g}{\partial t} + \frac{\partial \dot{m}_g}{\partial x} = -\frac{\partial \rho_s}{\partial t} \tag{6}$$

Assuming quasi-steady flow toward the surface,

$$\dot{m}_g = \int_0^x \frac{\partial \dot{m}_g}{\partial x'}\,\mathrm{d}x' = -\int_0^x \frac{\partial \rho_s}{\partial t}\,\mathrm{d}x' \tag{7}$$

Pyrolysis gases that are transported through the TPS are assumed to be in local thermal equilibrium with the surrounding solid.

Thermodynamic properties of the pyrolysis gas phase (i.e., density, enthalpy, and internal energy) are calculated as a function of temperature but at constant pressure. Naturally, the production of pyrolysis gases in the TPS will produce pressure gradients, which drive gaseous species toward the surface and, in higher dimensions, other regions of the TPS. Resolving these pressure gradients, however, requires an accounting of momentum conservation in the gas phase. For 1D systems, this level of fidelity is only expected to marginally improve the accuracy of the reconstruction algorithm, but with substantial added effort. Thus, momentum conservation of the gas phase will not be considered in this work.

Finally, it should be noted that Eq. (1) is defined for a fixed coordinate system and geometry and, thus, does not consider recession of the TPS. During atmospheric entry, accurate modeling of the TPS recession behavior requires detailed a priori knowledge of the external entry environment and boundary-layer composition; thus, the IHT problem would become underdefined. For this reason, recession is typically neglected even when using state-of-the-art IHT codes for postflight analysis [4]. While not necessarily accurate for Earth entry applications, neglecting recession is a valid approximation for many high-profile space exploration missions that will either descend into nonoxidizing environments (e.g., Dragonfly or Uranus Orbiter and Probe) or have coatings that greatly inhibit TPS recession (e.g., polysiloxane coatings on the forebody heat shields of Mars 2020 and Mars Science Laboratory [23,24]). For reconstructions of backshell heating conditions, the assumption of negligible surface recession is generally valid based on the heat rates these areas are expected to experience [4]. Thus, the level of fidelity captured by Eqs. (1) and (5) is applicable to a wide range of mission architectures of interest to the space exploration community.

2. Pretreatment of the Governing Heat Conduction Equation

To model the material response of the TPS via the Green's function framework, Eq. (1) must be linearized. To eliminate the nonlinear terms produced by expansion of the divergence term on the left-hand side of Eq. (1), a multiparameter Cole–Hopf transform is introduced:

$$\{T,\chi\} = \{f_1(\theta), f_2(f_1(\theta))\} \tag{8}$$

In Eq. (8), T represents the temperature change from an initial reference temperature $T = \tilde{T} - \tilde{T}_0$, and θ is introduced as a transformation variable (hereafter referred to as the *transformed temperature*). The transformation in Eq. (8) must satisfy the following condition:

$$\left[k\frac{\partial^2 f_1}{\partial\theta^2} + \frac{\partial k}{\partial f_1}\left(\frac{\partial f_1}{\partial\theta}\right)^2 + \frac{\partial k}{\partial f_2}\frac{\partial f_2}{\partial f_1}\left(\frac{\partial f_1}{\partial\theta}\right)^2\right] = 0 \tag{9}$$

which arises after substituting Eq. (8) into Eq. (1) and expanding. Equation (9) is itself a chain-rule expansion of the following homogeneous differential equation:

$$\frac{d}{d\theta}\left[k(\tilde{T},\chi)\frac{\partial f_1}{\partial\theta}\right] = 0 \tag{10}$$

which is integrated to yield

$$k(\tilde{T},\chi)\frac{\partial f_1}{\partial\theta} = A \tag{11}$$

In Eq. (11), A is an arbitrary constant. Equation (11) defines the required behavior for the transformation between T and χ, and θ. To accommodate the linear transformation from $\tilde{T}$ to T, the thermal conductivity $k(\tilde{T},\chi)$ is defined relative to a reference thermal conductivity value $k_0 = k(\tilde{T}_0, 0)$ as a function of the temperature change T:

$$k(\tilde{T},\chi) = k_0 + k_T(T,\chi) \tag{12}$$

It is important to recognize from Eq. (11) that f_1, and the associated inverse transformation $\theta = f_1^{-1}(T)$, has no closed-form solution, which is in contrast to the conventional Cole–Hopf transformation, where only the temperature dependence of the thermal conductivity is considered [21,25]. Instead of defining f_1 and f_2 explicitly, it is preferred to define an approximate inverse transformation:

$$\theta = \frac{1}{A}\left(1 + \beta\frac{\rho_c}{\rho_s}\chi\right)\int_0^T [k_0 + k_T(T',0)]\,\mathrm{d}T' \tag{13}$$

where β is a constant that best satisfies the condition in Eq. (11) for a local temperature time history. The procedure used to determine β is detailed in the Appendix. In the limit as $\beta \to 0$, Eq. (13) reduces to a single-parameter Cole–Hopf transformation defined for the virgin TPS. Thus, Eq. (13) can be considered a modification of the virgin material single-parameter Cole–Hopf transformation, scaled using the term enclosed in parentheses to capture the effects of decomposition. Uniqueness of the transformation from θ to T and χ is obtained by marching forward in time starting from initial conditions, using the solutions of T and χ from the previous time step as initial guesses, and is aided by the strong dependence of χ on the local temperature time history and the irreversible behavior of the TPS decomposition reaction.

As a result of the multiparameter Cole–Hopf transform, the transformed heat conduction equation becomes

$$\frac{1}{\alpha(\tilde{T},\chi)}\frac{\partial\theta}{\partial t} - \frac{\partial^2\theta}{\partial x^2} = \frac{g(x,t)}{A} \tag{14}$$

To fully linearize Eq. (14), the thermal diffusivity $\alpha(\tilde{T},\chi)$ is expanded relative to a reference value $\alpha_0 = \alpha(\tilde{T}_0, 0)$ as a function of the temperature change T:

$$\alpha(\tilde{T},\chi) = \alpha_0 + \alpha_T(T,\chi) \tag{15}$$

which, after substituting into Eq. (14) and rearranging, yields the following linear, inhomogeneous partial differential equation:

$$\frac{1}{\alpha_0}\frac{\partial\theta}{\partial t} - \frac{\partial^2\theta}{\partial x^2} = \frac{g'(x,t)}{A} \tag{16}$$

In Eq. (16), all nonlinear effects due to temperature- and composition-dependent thermophysical properties and pyrolysis are captured either within the multiparameter Cole–Hopf transformation or the virtual source term g', where

$$\frac{g'(x,t)}{A} = \frac{\alpha_T(T,\chi)}{\alpha_0}\frac{\partial^2\theta}{\partial x^2} + \frac{\alpha_0 + \alpha_T(T,\chi)}{\alpha_0}\frac{g(x,t)}{A} \tag{17}$$

3. Green's Function Solution Equation

Once pretreated into the form given by Eq. (16), the solution to the governing heat conduction equation at the temperature probe location can be accessed via the Green's function solution equation [18,20,21]. Within the Green's function formalism, the transformed TPS temperature is represented as a sum of two integrals:

$$\theta(x,t) = -\int_0^t \frac{\alpha_0}{A} q_{\mathrm{HW}}(\tau) G(x,t,L,\tau)\,\mathrm{d}\tau + \int_0^t \int_0^L \frac{\alpha_0}{A} g'(x_0,\tau) G(x,t,x_0,\tau)\,\mathrm{d}x_0\,\mathrm{d}\tau \tag{18}$$

The first integral term on the right-hand side of Eq. (18) captures the contributions of the net hot-wall heat flux conducted into the TPS q_{HW}, where G represents the Green's function of the TPS domain and A is the constant defined in the multiparameter Cole–Hopf transform [Eq. (11)]. Within the multiparameter Cole–Hopf transformation, q_{HW} is related to $\partial\theta/\partial x$ at the surface via

$$q_{\mathrm{HW}} = -A\frac{\partial\theta}{\partial x} \tag{19}$$

which is analogous to Fourier's law. The second integral on the right-hand side of Eq. (18) captures the effects of pyrolysis, internal gas transport, and nonlinear thermophysical properties. It should be noted that, while the 1D model system (Fig. 1) contains additional domains for the adhesive layer and substructure, these components do not pyrolyze and are modeled using constant material properties; thus, they are not included in the volumetric integral in Eq. (18).

In this work, the TPS domain Green's function $G(x,t,x_0,\tau)$ is constructed using a finite sum of eigenfunctions approximated with the Galerkin method. Adapted from [18,21],

$$G(x,t,x_0,\tau) = \sum_{n=1}^{N} \frac{k_0}{\alpha_0}\phi_n(x)\phi_n(x_0)e^{-\Lambda_{n,n}(t-\tau)} \tag{20}$$

In Eq. (20), $\Lambda_{n,n}$ represents the eigenvalue accompanying each TPS-domain eigenfunction ϕ_n. The eigenfunctions correspond to those that form the homogeneous solution of Eq. (16), where each ϕ_n is approximated using an N-ordered set of scaled basis functions $\hat{\boldsymbol{f}}$:

$$\phi_n = \sum_{j=1}^{N} \psi_{j,n}\hat{f}_j \tag{21}$$

In Eq. (21), basis functions $\hat{f}_j$ are required to satisfy the homogeneous boundary (e.g., an adiabatic internal surface) and interface continuity conditions of the model system. Basis functions are scaled by the eigenvector $\boldsymbol{\psi}_n$ accompanying each eigenfunction ϕ_n. Eigenvalues $\Lambda_{n,n}$ and eigenvectors $\boldsymbol{\psi}_n$ in Eqs. (20) and (21) are calculated using the approach described in [19]. It should be noted that, due to the linearization of the governing heat conduction equation into the form of Eq. (16), eigenvectors and eigenvalues are calculated only once, typically after the model system, material properties, and reference temperature are defined. Thus, the construction of the TPS Green's function accounts for a minimal portion of the total reconstruction cost.

Finally, it is important to emphasize that, while the eigenvalues and eigenvectors are defined *globally* for the entire model system, basis functions and, consequently, the eigenfunctions are defined *locally* for each domain; in the TPS domain, the effects of the adhesive layer and substructure on the TPS material response are captured within the behavior of the basis functions $\hat{f}_j$, considering continuity of temperature and heat flux across interfaces. Basis functions for the multimaterial 1D model system (Fig. 1) are detailed in the Supplemental Material.

B. Recovery of the Net Hot-Wall Heat Flux

In the second step of the reconstruction algorithm, the net hot-wall heat flux is recovered from the Green's function formulation of the TPS thermal response. The net hot-wall heat flux is first isolated from all other quantities in Eq. (18):

$$\theta(x,t) - g_{\mathrm{tot}}(x,t) = -\int_0^t \frac{\alpha_0}{A} q_{\mathrm{HW}}(\tau) G(x,t,L,\tau)\,\mathrm{d}\tau \tag{22}$$

where $g_{\mathrm{tot}}(x,t)$ represents the integrated source term:

$$g_{\mathrm{tot}}(x,t) = \int_0^t \int_0^L \frac{\alpha_0}{A} g'(x_0,\tau) G(x,t,x_0,\tau)\,\mathrm{d}x_0\,\mathrm{d}\tau \tag{23}$$

For measurements sampled at a finite rate, Eq. (22) is recast as a discrete linear system [20]:

$$\boldsymbol{\theta} - \mathbf{g_{tot}} = -\frac{\alpha_0}{A}\mathbf{G}\mathbf{q_{HW}} \tag{24}$$

which is then inverted to solve for q_{HW}.

Direct inversion of the linear system in Eq. (24), however, is ill-posed and prone to instabilities if noise is present in the input temperature measurement. These instabilities are usually mitigated via regularization, where minimization of the solution residual is balanced with the addition of a penalty function [26]. It is important to note that, while the Green's function formulation and choice of regularization approach are not mutually dependent, the regularization method must be chosen carefully so as not to adversely impact the reconstructed heating solution. The most common regularization approach used for IHT problems is Tikhonov regularization, where the penalty function minimizes the squared l_2-norm of the solution itself [27]. However, while Tikhonov regularization generally yields high-quality reconstructed heating solutions [4], it does require identification of optimal user-defined tuning parameters and, in some instances, can oversmooth sharp solution features [26].

Alternatively, when data from a heat flux sensor in proximity to the temperature probe is available, the sensor fusion approach proposed in [28] can be leveraged to stabilize the inversion of Eq. (24). Such sensor configurations were included on the backshell of the Mars 2020 [1] and Dragonfly [29] entry spacecraft and on many ground test articles [6]. The sensor fusion-based regularization approach has been shown to preserve sharp solution features in high-noise measurement scenarios and is generally less susceptible to suboptimal choices of user-input regularization parameters versus conventional techniques [28]. Thus, when applicable, the sensor fusion approach will be the preferred method to stabilize the inversion of Eq. (24).

When θ and g_{tot} are well defined, the solution of q_{HW} can be accessed directly via the least-squares solution of Eq. (24). The parameter g_{tot}, however, is initially unknown and must be calculated using iterative solutions of q_{HW}. The iterative solution process is shown schematically in Fig. 2. For each iteration of q_{HW}, a Gaussian quadrature scheme is used to approximate g_{tot} by calculating the integrand term in Eq. (23) at a small number N_x of discrete locations ξ_i within the TPS [30,31]:

$$\int_0^L g'(x_0,\tau)G(x,t,x_0,\tau)\,\mathrm{d}x_0 = \int_{-1}^{1} g'(\xi_0,\tau)G(\xi,t,\xi_0,\tau)\frac{L}{2}\,\mathrm{d}\xi_0 \approx \frac{L}{2}\sum_{i=1}^{N_x} w_i g'(\xi_i,\tau)G(\xi,t,\xi_i,\tau) \tag{25}$$

where w_i are standard Gaussian quadrature weights and ξ_i are the roots of the N_x-order Legendre polynomial. In Eq. (25), ξ is mapped to x through transformation of the TPS domain from $x \in [0, L]$ to $\xi \in [-1,1]$. The components of g' at each integration point ξ_i are derived from the local solutions of θ, $\partial\theta/\partial x$, or $\partial^2\theta/\partial x^2$, which are efficiently calculated using Eq. (18), or its derivatives with respect to x, evaluated at ξ_i. Note again that the Green's function defined in Eq. (20) is valid for all locations in the TPS. The local solution of θ is transformed to yield T and χ via numerical inversion of Eq. (13). At each integration point, $\partial T/\partial x$ is computed using the Fourier's law analog defined by Eq. (19):

$$k(\tilde{T},\chi)\frac{\partial T}{\partial x} = A\frac{\partial\theta}{\partial x} \tag{26}$$

The quantities T, χ, and $\partial T/\partial x$ are then used to compute all other parameters in g' for each integration point. Lastly, it is worth noting that, because T, χ, and $\partial T/\partial x$ are all quantities that are calculated using the reconstructed heat flux boundary condition, they can, in theory, be calculated using any material response solver of choice. In the current reconstruction algorithm, the Green's function approach was used to calculate the quantities in g' for efficiency and to keep the algorithm self-contained.

C. Aeroheating Environment Reconstruction

In the final step of the reconstruction algorithm, the solution of q_{HW} is used to predict the heat flux absorbed by the TPS solely from the aeroheating environment. At the surface, multiple heat transfer mechanisms contribute to q_{HW} via the surface energy balance:

$$q_{\text{HW}} = q_{\text{conv}} + \alpha_s q_{\text{rad}} - \epsilon_s\sigma_{\text{SB}}(\tilde{T}_s^4 - \tilde{T}_\infty^4) \tag{27}$$

In the right-hand side of Eq. (27), the first term represents the convective heat flux through the viscous boundary layer. The second term represents the absorbed heat flux from the shock layer radiation, where α_s is the absorptivity of the TPS surface and q_{rad} is the total radiative flux incident on the TPS. The third term

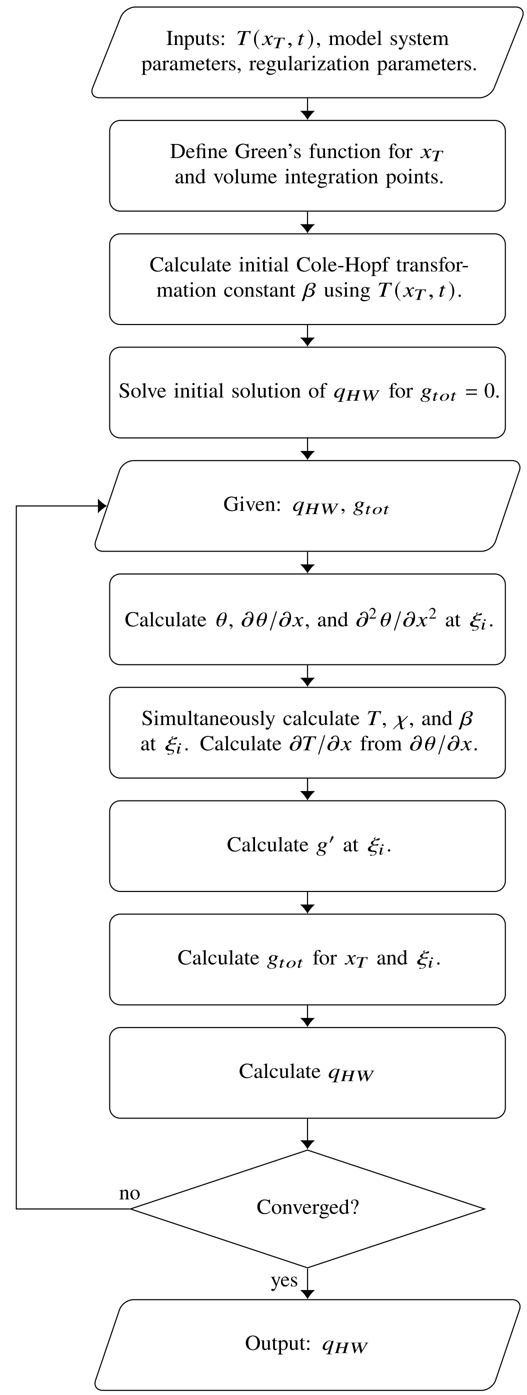

Fig. 2 Flowchart for the reconstruction algorithm.

represents the radiative emission from the TPS, where ϵ_s is the emissivity of the TPS surface, σ_{SB} is the Stefan–Boltzmann constant, $\tilde{T}_s$ is the TPS surface temperature, and $\tilde{T}_\infty$ represents the background temperature.

The heat flux imposed by the aerothermal environment during atmospheric entry is represented by the sum of the first two terms on the right-hand side of Eq. (27), which will be referred to hereafter as the *incident heat flux* q_{inc}. To recover q_{inc}, q_{HW} is corrected by the radiative emission from the TPS surface, such that

$$q_{\text{inc}} = q_{\text{HW}} + \epsilon_s\sigma_{\text{SB}}(\tilde{T}_s^4 - \tilde{T}_\infty^4) \tag{28}$$

where the emissivity of the TPS depends on both temperature and composition [11]:

$$\epsilon_s(\tilde{T},\chi) = (1-\chi)\frac{\rho_v}{\rho_s}\epsilon_v(\tilde{T}) + \chi\frac{\rho_c}{\rho_s}\epsilon_c(\tilde{T}) \tag{29}$$

The surface temperature $\tilde{T}_s$ and char fraction are calculated via Eq. (18) evaluated at the surface using the converged solution of q_{HW}.

D. Computation Cost

The total cost of the reconstruction algorithm is sensitive to the size of the measurement time series N_t and the order of the numerical integration scheme N_x used to approximate g_{tot}. In the limiting case, when the effects of pyrolysis and nonlinear material properties are negligible, the total algorithm cost is dominated by the least-squares solution of q_{HW} in Eq. (24). This operation is purely sensitive to N_t. As pyrolysis effects become more significant, the iterative solution of q_{HW} begins to drive the total reconstruction cost, notably due to both the calculation of g' for N_x integration points, as well as the least-squares solution of q_{HW} for each iteration. Nonetheless, most steps in the reconstruction algorithm consist of basic matrix operations that can be efficiently solved with minimal computing resources. For the reconstruction of the Mars 2020 atmospheric entry heating conditions (Sec. IV.B), which considers an input measurement time series with $N_t = 600$ sample points and an $N_x = 14$ order numerical integration scheme, the reconstruction algorithm routinely converges in less than 8 s with fewer than 10 iterations using MATLAB™ on a consumer-grade laptop computer with access to up to 8 CPU cores. By comparison, conventional time-marching-based IHT methods generate solutions for the same number of sample points in approximately 30 min using state-of-the-art computing clusters and significant code optimization [4,5].

III. Numerical Verification

A computational verification test case was constructed to analyze the accuracy of the reconstruction algorithm in an atmospheric entry heating scenario. Using a simulated temperature probe measurement in response to prescribed boundary conditions, the objective of the reconstruction algorithm is to recover the TPS surface heating conditions, surface temperature, and through-thickness material response [i.e., components of g' in Eq. (17)] in close agreement with results from a high-fidelity material response code, which will be referred to as the *reference solution*. The heat shield stack-up and associated parameters used in the verification test case are summarized in Table 1. The TPS was modeled using the Theoretical Ablative Composite for Open Testing (TACOT) material database [32], with no surface recession. The adhesive was modeled as HT424, and the substructure was modeled as aluminum with a reduced density and thermal conductivity to emulate a honeycomb configuration (34 $\mathrm{kg/m^3}$). The temperature probe was placed in the TPS domain at a depth of 0.254 cm from the external surface.

Table 1 Numerical verification heat shield stack-up parameters

Component	Material	Thickness, cm	Note
TPS	TACOT	3.0	No recession
Adhesive	HT424	0.14	Constant properties
Substructure	Aluminum honeycomb	1.27	Constant properties

Initially, the system is held at a uniform temperature and pressure of 300 K and 10 kPa, respectively. In the verification scenario, the external surface of the TPS is exposed to a combined convective and radiative heat pulse (Fig. 3a). Throughout the heat pulse, the film coefficient C_H and incident radiative heat flux q_{rad} are modulated as a sine wave. The pressure at the external surface of the TPS remains fixed at 10 kPa and the bulk enthalpy is fixed at 1 MJ/kg. The TPS-embedded temperature probe measurement (Fig. 3b) and reference surface heat flux, surface temperature, and through-thickness material response solutions were calculated using the Porous Material Analysis Toolbox based on OpenFOAM (PATO) [33]. In the reconstruction algorithm, a basis function order of $N = 12$ was used to construct Green's function [Eq. (20)], and a numerical integration order of $N_x = 36$ was used to evaluate g_{tot} in the TPS domain [Eq. (23)]. Because the heating conditions are smoothly varying and the input measurements do not contain noise, Tikhonov regularization was used to stabilize the solution [26].

The results of the verification test case are shown in Fig. 4. Reconstructed net hot-wall and incident heating profiles are shown in Fig. 4a, and the reconstructed surface temperature is shown in Fig. 4b. In Fig. 4a, the blue line represents the net hot-wall heat flux q_{HW}, and the orange line represents the incident heat flux q_{inc} [Eq. (28)]. Reconstructed heat flux profiles using the Green's function approach are shown as solid lines, and PATO-generated outputs (i.e., the reference solution) are shown as dashed lines.

The reconstruction algorithm recovers the TPS surface heating conditions in good agreement with the reference solution. The approach is accurate to within 5% throughout the significant heating region ($t = 45$ to 90 s), with errors of 2% for both the peak net hot-wall and incident heat flux values. The surface temperature rise from the initial conditions is reconstructed to within 1% of the PATO reference solution.

The reconstructed through-thickness material response is compared next against the reference solution to assess the algorithm's ability to capture global heat conduction and thermophysical phenomena in pyrolyzing TPS materials. Figure 5 compares the through-thickness temperature distribution (Fig. 5a) and decomposition, represented as $1-\chi$ (Fig. 5b), for every third integration point in the numerical solution of g_{tot}. Similar to the reconstructed surface heat flux and temperature, the through-thickness material response is captured in excellent agreement with the reference solution.

A. Numerical Integration Resolution

Due to the highly nonlinear behavior and numerical stiffness of the TPS decomposition reaction, accurate reconstructions that

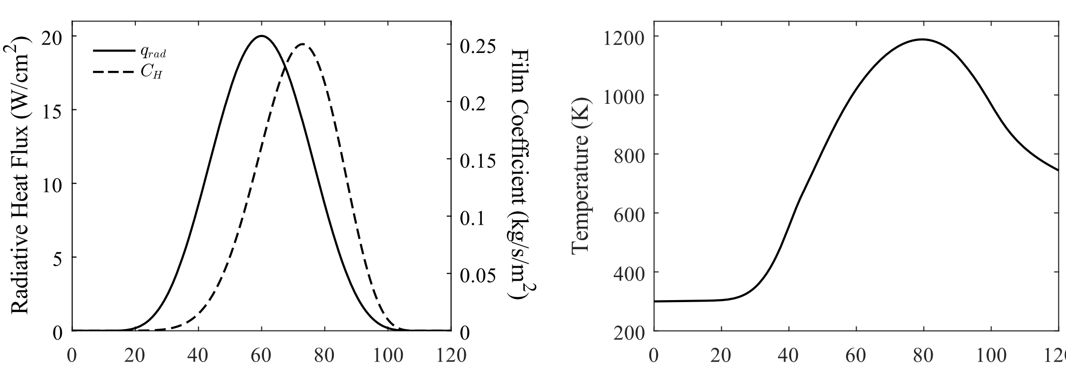

Fig. 3 Numerical verification inputs. a) Radiative (solid line) and convective (dashed line) boundary conditions imposed on the 1D model system. b) Simulated temperature probe measurement.

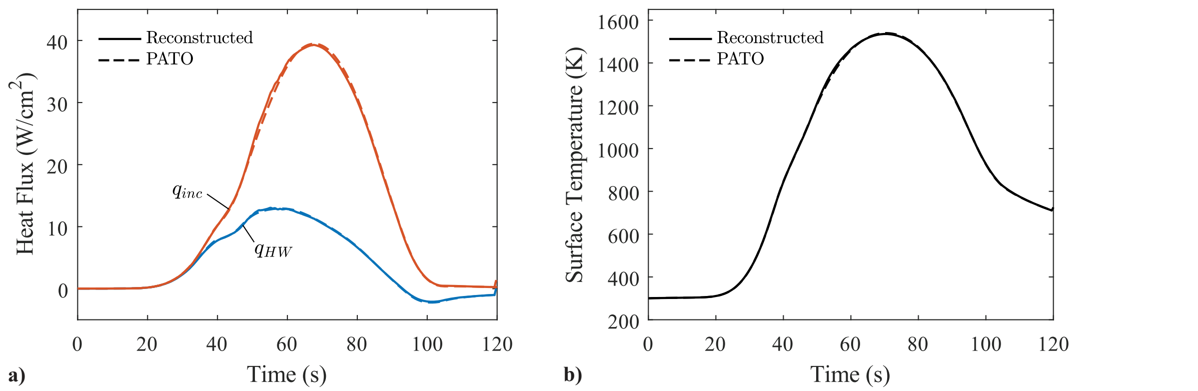

Fig. 4 Numerical verification results. a) Reconstructed net hot-wall and incident heat flux. b) Reconstructed surface temperature. Reference solutions are shown by the dashed lines.

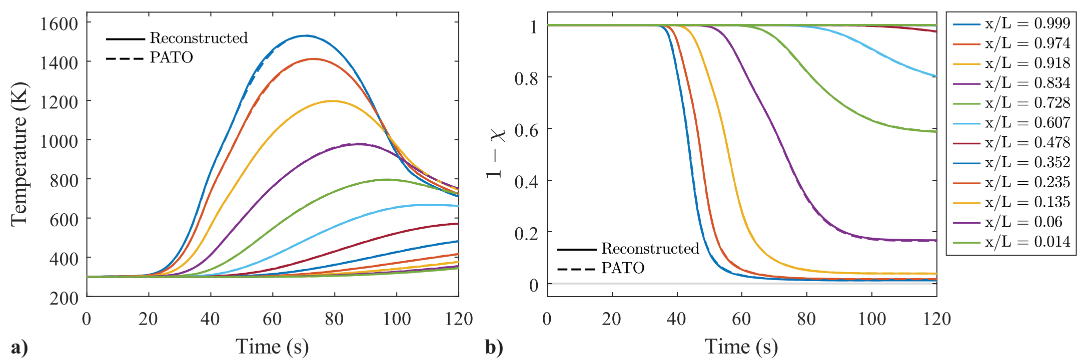

Fig. 5 Numerical verification results. a) Reconstructed through-thickness temperature. b) Reconstructed decomposition. The temperature probe is located at $x/L = 0.915$. Reference solutions are shown by the dashed lines.

consider the effects of pyrolysis and internal convection require adequate resolution of numerical integration points near the surface. If the resolution of the numerical integration scheme is coarse relative to the length scale of the decomposition front (typically designated as the region where $0.02 < \chi < 0.98$), sharp spatial variations in $\partial\rho_s/\partial t$ can lead to large nonphysical oscillations in the pyrolysis gas mass flux [Eq. (7)], negatively impacting the reconstruction accuracy.

Figure 6 shows the reconstructed heating conditions (Figs. 6a–6d) and pyrolysis gas mass flux at the TPS surface (Figs. 6e–6h) for four

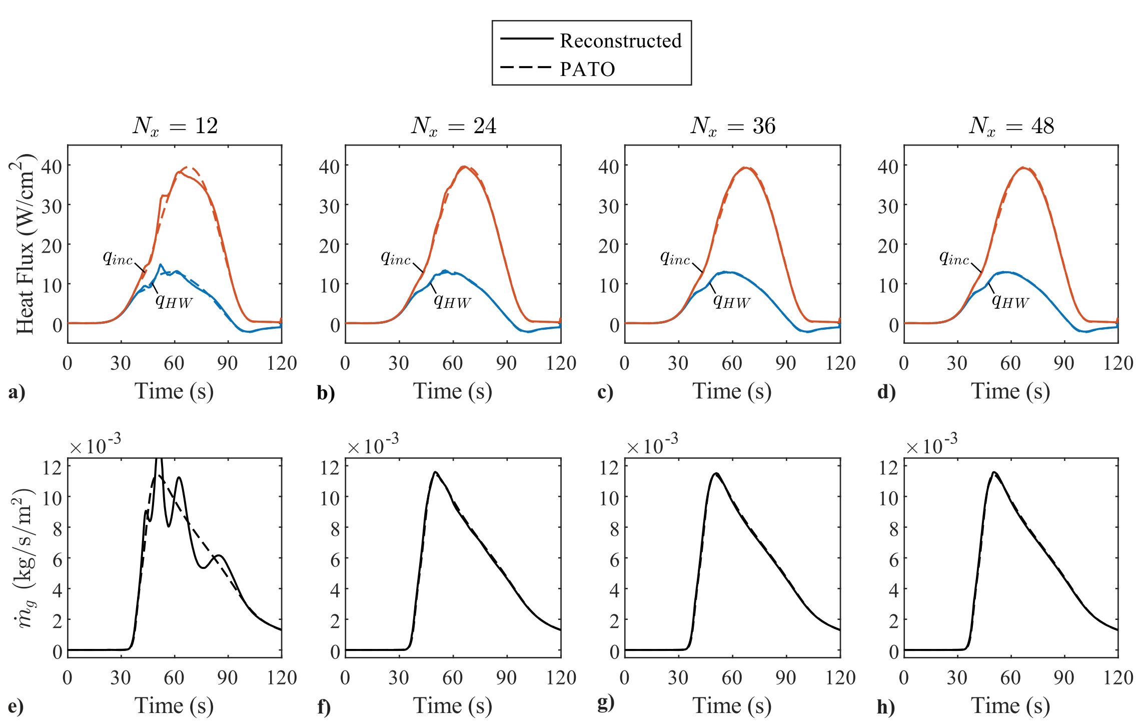

Fig. 6 Reconstructed solutions for various numerical integration orders N_x. a-d) Reconstructed surface heating conditions. e-h) Reconstructed pyrolysis gas mass flux at the TPS surface. Reference solutions are shown by the dashed lines.

Table 2 Total computation time for various numerical integration orders N_x

N_x	Computation time, s
12	9.2
24	14.2
36	23.1
48	34.9

Table 3 Total computation time for various Galerkin basis function orders N

N	Computation time, s
3	17.7
6	21.6
9	20.8
12	23.1

different values of N_x. Gaussian quadrature schemes generate exact integral solutions for polynomials of order $2N_x - 1$ or less [30,31]. Thus, the lowest value of $N_x = 12$ is the minimum numerical integration order that would yield an exact solution to the integral of the Green's function (approximated using a 22nd-order polynomial for $N = 12$) in g_{tot}, assuming no spatial variation in g'.

Large oscillations are visible in the solution at the lowest quadrature order (Figs. 6a and 6e), which become progressively smoothed as the resolution of the numerical integration scheme increases. Beyond a numerical integration order of $N_x = 36$, representative of the verification results shown previously, the reconstructed heating conditions and material response become insensitive to refinement. Solution times for the four reconstructions shown in Fig. 6, calculated using a consumer-grade PC, are tabulated in Table 2. The increase in computation time demonstrates that, for the same-sized measurement time series, the total cost of the reconstruction algorithm becomes highly dependent on the number of integration points required to accurately calculate g_{tot}.

B. Galerkin Basis Function Order

In prior work, the criterion for the minimum order N of the Galerkin basis function set used to approximate the Green's function was established using the dimensionless thermal penetration depth [28]:

$$\alpha_0 t_m/(L - x_T)^2 \tag{30}$$

where t_m is the characteristic time of the measurement time series. Considering a characteristic measurement time equal to half of the test scenario time (i.e., $t_m = 60$ s), the parameter $\alpha_0 t_m/(L - x_T)^2$ is equal to 13.4. From [28], it is expected that the Green's function approach will yield accurate solutions when $N \geq 5$ under these conditions. Reconstructed heating conditions for four different values of the Galerkin basis function order N are shown in Fig. 7. For all reconstructions in Fig. 7, a numerical integration order of $N_x = 36$ was used.

The results in Fig. 7 are consistent with the criteria outlined in [28]. For Galerkin basis function orders of $N = 6$ and above, the reconstructed heating solutions are indistinguishable. However, in contrast with the behavior of increasing the numerical integration order, there is no significant increase in computation time when increasing the Galerkin basis function order, as shown in Table 3. In fact, for solutions using higher-order basis functions ($N \geq 9$), the computation time decreases due to faster convergence. Thus, as long as the basis function order N is above the minimum threshold, the precise choice of N is unlikely to have a considerable impact on the solution quality and speed.

Overall, these numerical verification results demonstrate a first-of-its-kind application of the Green's function framework for reconstructing the heating conditions on ablative TPS materials. Subject to representative atmospheric entry heating conditions, the approach is accurate to within 5% of the high-fidelity reference solution and can adequately capture the effects of decomposition and internal convection on the material response. Notably, the results highlight the versatility of the Green's function formalism and position it well for adaptation to other highly nonlinear material systems where conventional modeling techniques become computationally expensive.

IV. Aeroheating Reconstruction Using Ground Test and Flight Data

Experimental measurements were used to validate the Green's function reconstruction algorithm and benchmark its performance against the current state-of-the-art inverse heat transfer code, FIAT_Opt. The data sets used were generated from both ground testing and flight missions. These include measurements from arc-jet test articles in the Panel Test Facility (PTF) at NASA Ames and from the backshell of the Mars 2020 atmospheric entry spacecraft. In all scenarios, measurements were sampled in regions with collocated heat flux sensor and temperature probe instrumentation. Due to the availability of collocated heat flux sensor and temperature probe measurements, the sensor fusion regularization methodology [28] was used to stabilize the reconstruction. In all reconstructions, a Galerkin basis function order of $N = 12$ was used to construct the Green's function, and a numerical integration order of $N_x = 14$ was used to calculate g_{tot}. The choice of N satisfies the criteria outlined in [28], while the choice of N_x results in a resolution of integration points sufficient to resolve the decomposition front near the TPS surface.

A. Ground Test Validation

During the development and qualification of the Mars Entry, Descent, and Landing Instrumentation 2 (MEDLI2) sensor suite and TPS architecture used on the Mars 2020 spaceflight mission,

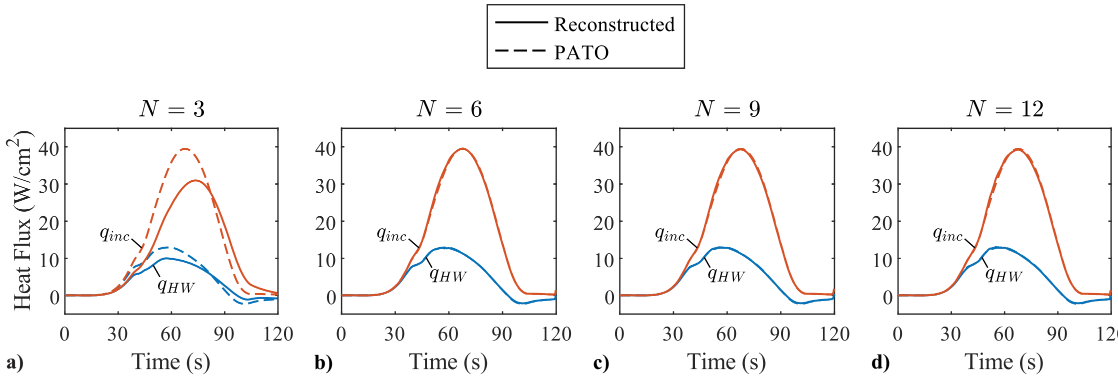

Fig. 7 Reconstructed solutions for various Galerkin basis function orders N. Reference solutions are shown by the dashed lines.

numerous panel arc-jet tests were performed in the Panel Test Facility at NASA Ames. PTF test campaign 162 consisted of four SLA-561V panels instrumented with a thermocouple (TC) plug, total heat flux sensor, and radiometer [6,34] (Fig. 8). The TC plug and heat flux sensor were positioned in an arrangement analogous to the collocated sensor pairs on the Mars 2020 backshell, separated by a distance of 10 cm along the spanwise flow direction. The sensors were sampled at a rate of 20 Hz (downsampled to 5 Hz in the Green's function reconstruction algorithm and 4 Hz in FIAT_Opt). The TPS test panels were coated with a white thermal control spray, except within a 5 cm radius of each heat flux sensor and TC plug, to mimic the Mars 2020 backshell configuration. Nominal test conditions are detailed in [34] and shown in Table 4. The first two tests represent low heating conditions, whereas the latter two tests represent high heating conditions.

Reconstructed heat flux profiles are shown in Fig. 9 for the low heating (Figs. 9a and 9b) and high heating (Figs. 9c and 9d) test conditions. Each figure displays the net hot-wall heat flux q_{HW} conducted into the solid and the incident heat flux q_{inc} from the arc-jet test environment [Eq. (28)], comparing the reconstructed heat flux profiles using the Green's function approach with those using FIAT_Opt. The plots also indicate the target cold-wall and adiabatic-wall heat flux values for each arc-jet test for comparison with the reconstructed incident heat flux.

Multiple stages of the arc-jet test sequence are evident in the heat flux profiles, including the tunnel startup, test article insertion (including initial transients), steady test period, and test article extraction phases (labeled in Fig. 9a). Most critical is the performance of the reconstruction algorithm during the steady test period, which begins at approximately $t = 45$ s and ends with a drop in the incident heating upon test article extraction. Throughout the steady test period, the net hot-wall heat flux decreases with time for all test scenarios as the TPS surface approaches an adiabatic-wall condition ($q_{\mathrm{HW}} = 0$). Across all test scenarios, the reconstruction algorithm predicts the net hot-wall and incident heat flux to within 12 and 6% of FIAT_Opt, respectively. In the low heating scenarios, both methods predict q_{inc} within the target cold-wall and adiabatic-wall bounds during the steady test period. In the high heating scenarios, both methods overpredict the target cold-wall heating conditions, by up to 15% using FIAT_Opt and up to 10% using the Green's function approach. It should be noted, however, that the stated uncertainty for the calibrated PTF cold-wall heat flux is $\pm 15\%$ [35]. Considering expanded cold-wall bounds due to facility calibration uncertainties, both reconstruction methods adequately predict the incident heating conditions in the high heating scenarios.

Table 4 PTF test campaign 162 run parameters [34]

Tests	Target adiabatic-wall heat flux, $\mathrm{W/cm^2}$	Target cold-wall heat flux, $\mathrm{W/cm^2}$	Steady test duration, s
1 and 2	4.3	5.4	63
3 and 4	8.6	9.7	25

The discrepancies between the incident heat flux calculated using the Green's function approach and FIAT_Opt are correlated with differences in the reconstructed surface temperatures $\tilde{T}_s$, notably for the high heating conditions. Figure 10 shows the reconstructed surface temperature profiles for all four tests. In the low heating conditions (Figs. 10a and 10b), the Green's function approach recovers the surface temperature to within 1% of FIAT_Opt during the steady test region, with only minor discrepancies during the transient test article insertion phase. In the high heating scenarios (Figs. 10c and 10d), the Green's function approach slightly underpredicts the TPS surface temperature, to within 2%, up to halfway through the steady test period (approximately at $t = 60$ s). In the latter half of the steady test period, the FIAT_Opt-reconstructed surface temperature is more dynamic and drops below that predicted by the Green's function approach, commensurate with the behavior of q_{inc} in Figs. 9c and 9d. While the difference in the reconstructed surface temperature between the two approaches is small compared to the overall temperature rise, the radiative emission from the hot TPS surface scales as a function of $\tilde{T}_s^4$. Thus, in scenarios with high heating rates, small discrepancies in the reconstructed surface temperatures become amplified in the calculation of q_{inc} [Eq. (28)].

B. Mars 2020 Backshell Reconstruction

The Mars 2020 atmospheric entry spacecraft flew an extensive set of TPS-embedded thermal instrumentation as part of the MEDLI2 sensor suite [1]. Among these were two pairs of collocated heat flux sensors and TC plugs located on the backshell shoulder region: the MTB01/MTB07 TC plug/heat flux sensor pair, embedded in the wind-side region of the backshell, and the MTB02/MTB08 sensor pair, embedded in the lee-side region of the backshell. Both sensor pairs are highlighted in Fig. 11. In the region of the sensors, the nominal thickness of the TPS was 1.27 cm [36]. Within each TC plug, the shallowest TC was placed at a nominal depth of 0.254 cm from the external TPS surface [4]. During atmospheric entry, measurements from the TC plugs and heat flux sensors were sampled at a rate of 8 and 16 Hz, respectively. For both the Green's function approach and FIAT_Opt, all measurements were downsampled to 4 Hz.

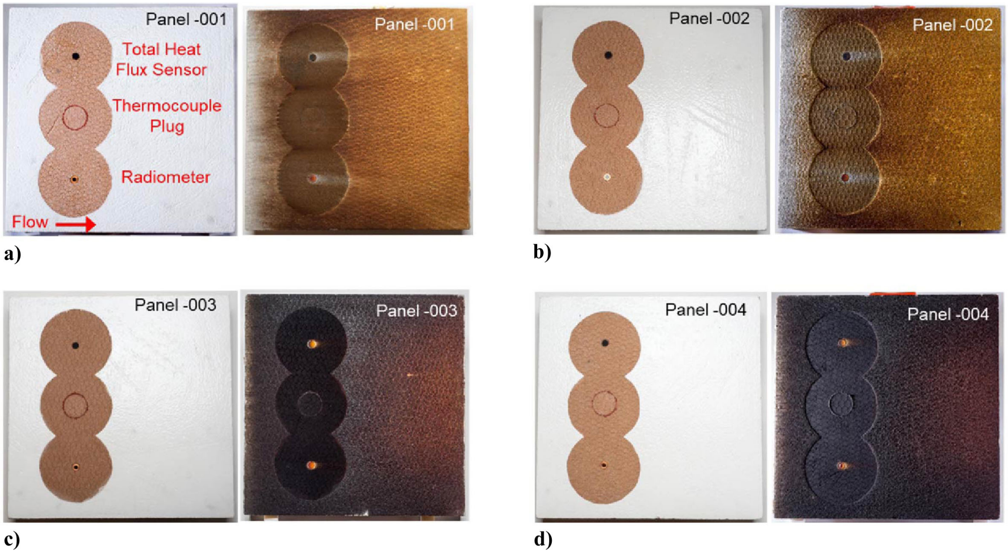

Fig. 8 Photographs of PTF test campaign 162 test articles before (left) and after (right) arc-jet exposure. a) Test 1. b) Test 2. c) Test 3. d) Test 4. Adapted from [6].

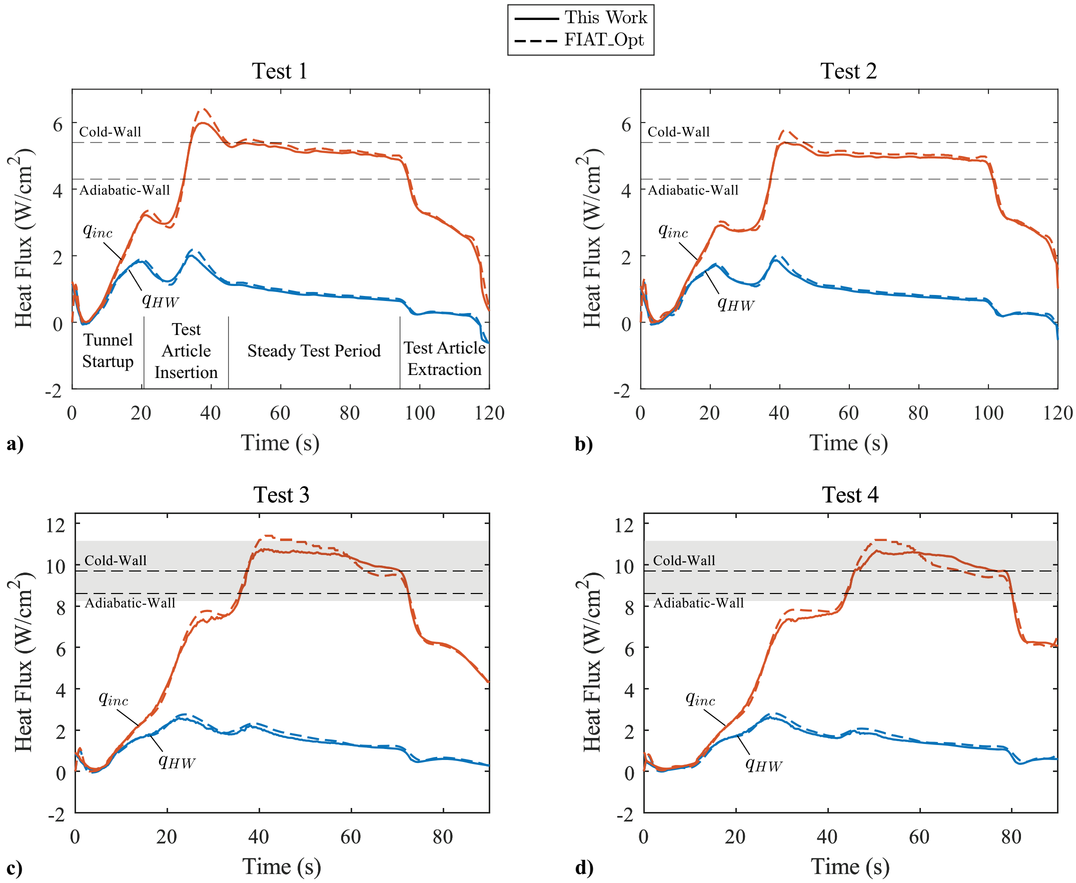

Fig. 9 Reconstructed net hot-wall (blue) and incident (orange) heating results for PTF test campaign 162. a) Test 1, b) Test 2, c) Test 3, and d) Test 4. The shaded regions in c) and d) represent ±15% facility calibration uncertainty margins [35].

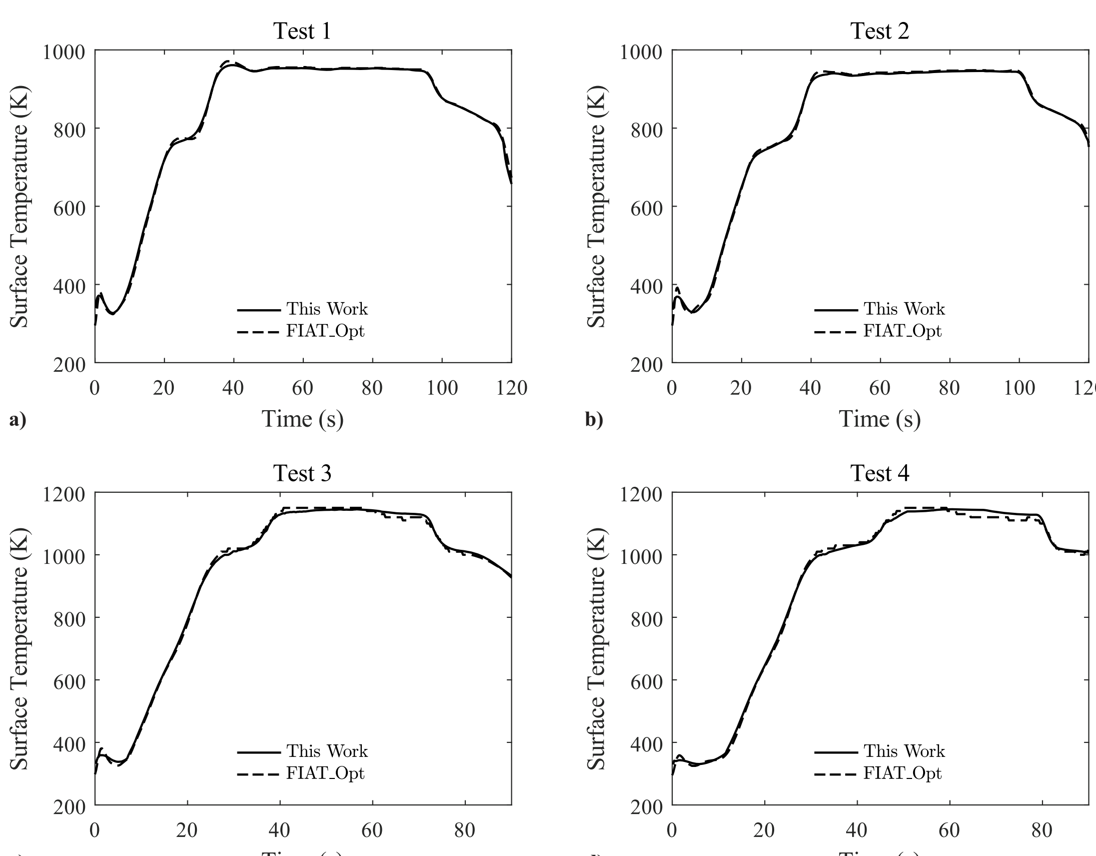

Fig. 10 Reconstructed surface temperatures for PTF test campaign 162. a) Test 1, b) Test 2, c) Test 3, and d) Test 4.

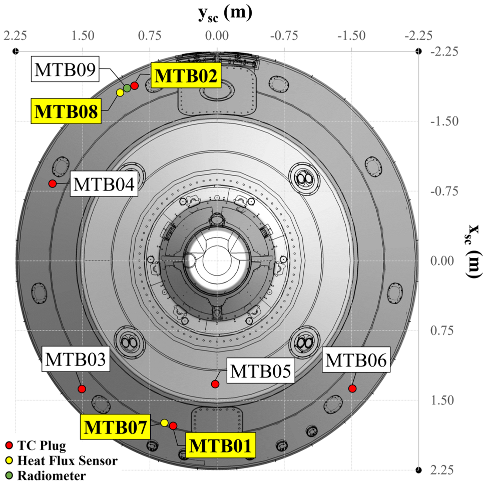

Fig. 11 Schematic of the Mars 2020 backshell (adapted from [1]). Highlighted sensor labels indicate those used in this work.

1. *Nominal Flight Reconstruction*

Reconstructed net hot-wall and incident heat flux profiles are shown in Fig. 12 for both sensor pairs. Using the Green's function approach, the results converged in less than 8 s versus over 30 min using FIAT_Opt [4]. Consistent with prior analysis, the MTB02/MTB08 sensor pair on the leeward side experienced the highest incident heating conditions on the backshell, with a reconstructed peak heat flux of 4.8 W/cm^2. For both sensor pairs, a bimodal peak region is present in the reconstructed incident heat flux, suggesting the presence of separate radiative and convective peak heating regimes.

The Green's function approach predicts a similar net hot-wall heat flux profile compared with FIAT_Opt, with peak values recovered to within 0.1 W/cm^2 for both sensor pairs. At the peak incident heating time, the Green's function approach overpredicts the FIAT_Opt-generated incident heat flux by 0.3 and 0.1 W/cm^2 for the MTB01/MTB07 and MTB02/MTB08 sensor pairs, respectively. The higher estimated peak incident heating using the Green's function approach is correlated with a higher reconstructed TPS surface temperature versus FIAT_Opt. Reconstructed surface temperature profiles using both approaches are shown in Fig. 13. For both sensor pairs, the Green's function approach overpredicts the surface temperature near the peak heating time by 23 and 8 K for the MTB01/MTB07 and MTB02/MTB08 sensor pairs, respectively. The amplification of the reconstructed surface temperature discrepancies in the calculation of q_{inc} can be explained in a similar fashion as in Sec. IV.A; i.e., the radiative emission from the TPS surface scales with $\tilde{T}_s^4$, amplifying small errors in T_s in the calculation of q_{inc}. Nonetheless, these results demonstrate that the Green's function-based reconstruction algorithm can capture the relevant heat conduction phenomena in atmospheric entry scenarios in close agreement with the state-of-the-art IHT methods and, notably, can compute such results in two orders of magnitude less time.

2. *Uncertainty Quantification*

In the postflight analysis of Mars 2020, Monte Carlo analyses were used to determine the uncertainty of the reconstructed heating conditions. While Monte Carlo simulations are sufficient to estimate the total reconstruction uncertainty, more detailed analyses are required to decompose the individual contributions of various input parameters to the total reconstruction uncertainty. These analyses are critical to guide materials characterization

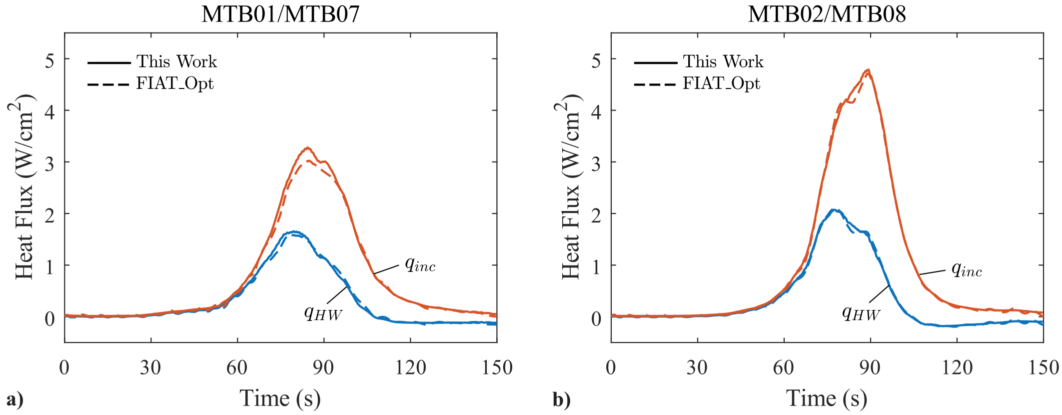

Fig. 12 Reconstructed heat flux profiles from the Mars 2020 backshell. a) Results from the MTB01/MTB07 sensor pair. b) Results from the MTB02/MTB08 sensor pair.

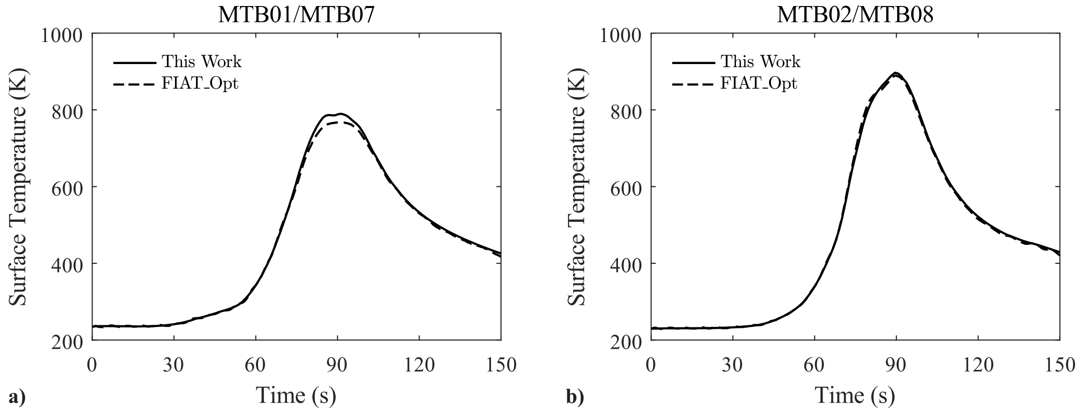

Fig. 13 Reconstructed surface temperatures from the Mars 2020 backshell. a) Results from the MTB01/MTB07 sensor pair. b) Results from the MTB02/MTB08 sensor pair.

efforts and reduce the margins of postflight-reconstructed atmospheric entry environments in the most cost-effective manner. Variance-based sensitivity analyses—such as the calculation of first-order or total Sobol indices—are often used to quantify input parameter uncertainty contributions [37]. As a metric, the total Sobol index of an input parameter is defined as the remaining model output variance when all other parameters are fixed, normalized by the total model variance [38]. More generally, the total Sobol index of a parameter can be considered as the fractional contribution of the uncertainty of that parameter to the total model output uncertainty. Due to the computational cost of such analyses, however, calculating total Sobol indices organically using FIAT_Opt simulations is not a practical endeavor. In prior work, a machine learning-based approach was implemented to overcome the computational burden by training a surrogate model to predict the peak heat flux and heat load at each TC plug location [4]. While this technique enabled the calculation of total Sobol indices with respect to the peak heat flux and heat load, the analyses did not give any insight with respect to other periods or features throughout the entry heat pulse.

Here, the Green's function approach is used to calculate the uncertainty of the reconstructed heating conditions, as well as total Sobol indices for each input parameter, throughout the entire atmospheric entry flight duration. Input parameter uncertainty distributions for the Mars 2020 flight lot backshell TPS and the embedded temperature probe are tabulated in Table 5. Uncertainty distributions in Table 5 are normalized by the mean value, unless otherwise noted, and are representative of those used in prior MEDLI2 postflight analyses [4]. For the TPS density, specific heat, and thermal conductivity, variations in the respective virgin and char properties are coupled using a single scaling distribution. For material properties that are bounded, such as emissivity, a truncated normal distribution was used to avoid nonphysical inputs.

Monte Carlo simulations (5000 samples) were used to compute the overall uncertainty of the reconstructed heating conditions. Resulting distributions of the reconstructed net hot-wall and incident heat flux for each sensor pair are shown in Fig. 14. In Fig. 14, the overall solution distribution is represented as a mean solution with a 95% confidence interval envelope ($\pm 1.96\sigma$) for both the net hot-wall (blue) and incident (orange) heat flux.

Table 5 Input uncertainty scaling parameters from [4]. Both uniform (U) and normal (N) distributions were used in this analysis

Parameter	ρ	C_p	ϵ_v	ϵ_c	k	x_T
Distribution	U	N	N[a]	N[a]	N	N
$2\sigma/\mu$	± 0.018[b]	0.15	0.15	0.15	0.13	0.0076 cm[c]

[a]Truncated normal distribution.
[b]Upper/lower bounds.
[c]Not normalized by mean.

At the peak heating time, the 95% confidence interval for the reconstructed incident heat flux spans 1.4 W/cm^2 for the MTB01/MTB07 sensor pair (Fig. 14a) and 2.1 W/cm^2 for the MTB02/MTB08 sensor pair (Fig. 14b), in good agreement with prior analysis [4]. In both sensor pairs, the largest variation in both q_{HW} and q_{inc} coincided with the respective peak heating times. The margins of the reconstructed heating conditions due to input parameter uncertainties are at least a factor of 5 greater than the discrepancies in the nominal solutions using each method (Fig. 12).

Next, total Sobol indices for the reconstructed heating conditions were calculated using the Monte Carlo estimator proposed in [39]:

$$S_{T,i} = \frac{1}{2}\frac{\sum_{j=1}^{N_s}[q(\mathbf{A_s})_j - q(\mathbf{A_B}^{(i)})_j]^2}{\sum_{j=1}^{N_s}[q(\mathbf{A_s})_j - q_0]^2} \tag{31}$$

In Eq. (31), $S_{T,i}$ is the total Sobol index for input parameter i, N_s represents the number of samples per input parameter, q represents the model output (either the net hot-wall or incident heat flux), and q_0 is the mean solution. The variables $\mathbf{A_s}$ and $\mathbf{A_B}^{(i)}$ are sampling matrices with dimensions of $N_s \times k_s$, where k_s is the number of input parameters. The matrix $\mathbf{A_B}^{(i)}$ is constructed by replacing column i in matrix $\mathbf{A_s}$ with column i in matrix $\mathbf{B_s}$, where $\mathbf{B_s}$ is an independent sampling matrix with the same dimensions as $\mathbf{A_s}$. Thus, for N_s samples, $N_s \times (k_s + 1)$ independent reconstructions are required.

Total Sobol indices were calculated at each time step during the entry heat pulse for the reconstructed net hot-wall and incident heat flux for both sensor pairs using $N_s = 5000$ samples per input parameter in Table 5 ($k_s = 6$). Convergence plots of the peak heating total Sobol indices for the MTB02/MTB08 sensor pair are shown in Fig. 15. For both q_{HW} and q_{inc}, total Sobol indices at the peak heating time were fully converged after approximately $N_s = 4000$ samples. Total Sobol indices for q_{HW} are plotted in Figs. 16 and 17 for the MTB01/MTB07 and MTB02/MTB08 sensor pairs, respectively. Likewise, total Sobol indices for q_{inc} are plotted in Figs. 18 and 19 for the MTB01/MTB07 and MTB02/MTB08 sensor pairs, respectively. In each plot, labeled data points at the respective peak heating times represent the total Sobol indices calculated using the machine learning approach described in [4].

For each sensor pair, total Sobol indices for q_{HW} (Figs. 16 and 17) remained relatively constant until the peak heating region, with the reconstruction uncertainty dominated by the uncertainty in specific heat ($S_{T,C_p} > 0.9$). At the peak of q_{HW}, total Sobol indices calculated using the current approach show good agreement with those calculated using the prior machine learning approach for both sensor pairs (solid circles in Figs. 16 and 17). Following the peak heating region, total Sobol indices vary drastically. As the heat pulse subsides, $S_{T,k}$ increases substantially, up to 0.95 at $t = 94$ s for both

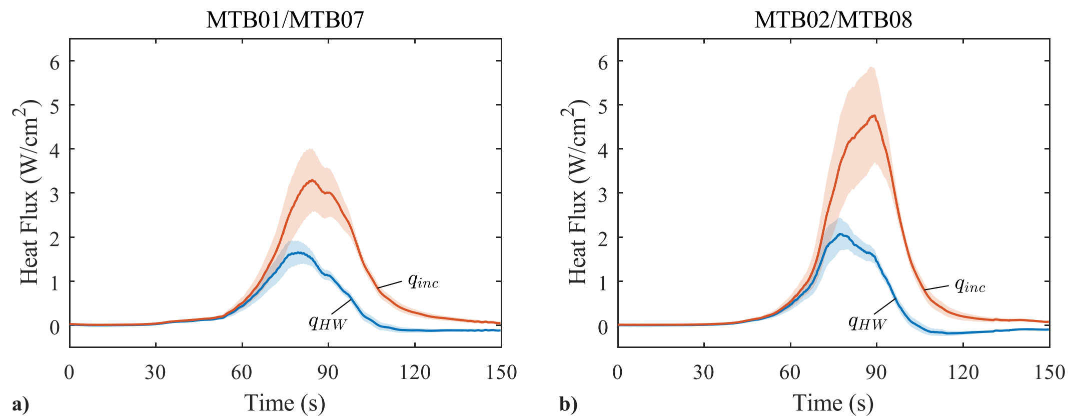

Fig. 14 Results of the Monte Carlo simulations for the a) MTB01/MTB07 and b) MTB02/MTB08 sensor pairs. The solid line represents the mean solution. The shaded envelope represents a 95% confidence interval.

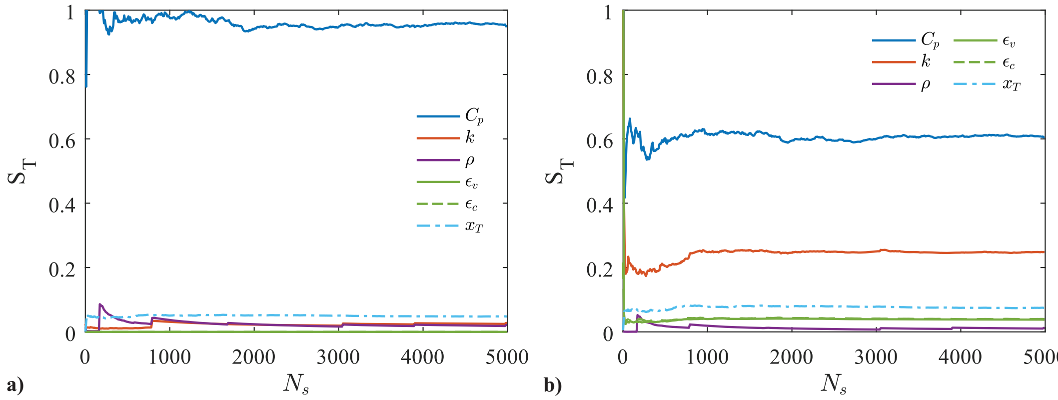

Fig. 15 Convergence plots of the peak heating total Sobol indices for the a) net hot-wall heat flux and b) incident heat flux for the MTB02/MTB08 sensor pair.

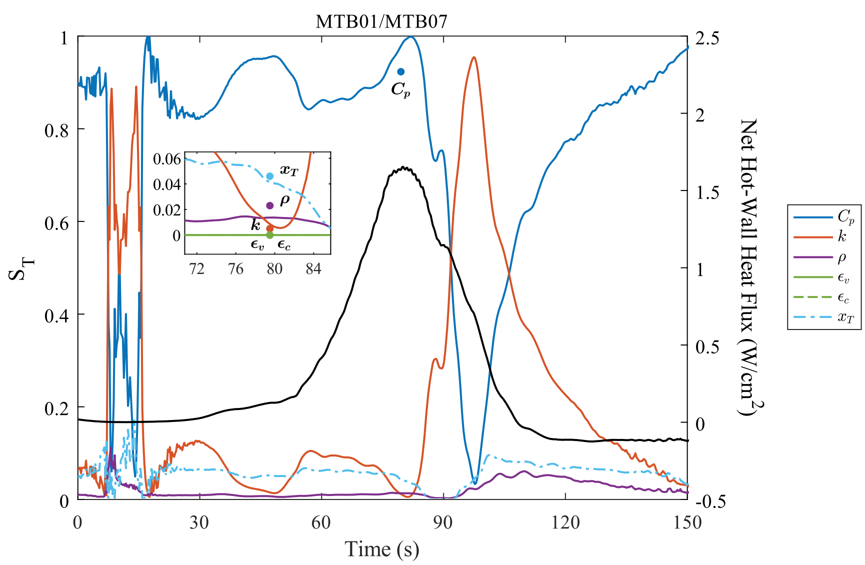

Fig. 16 Total Sobol indices for the reconstructed net hot-wall heat flux for the MTB01/MTB07 sensor pair. Labeled data points represent the total Sobol indices calculated in [4]. The solid black line is the nominal solution of q_{HW} from Fig. 12a. Inset: Magnified region for the total Sobol indices at the peak heating time.

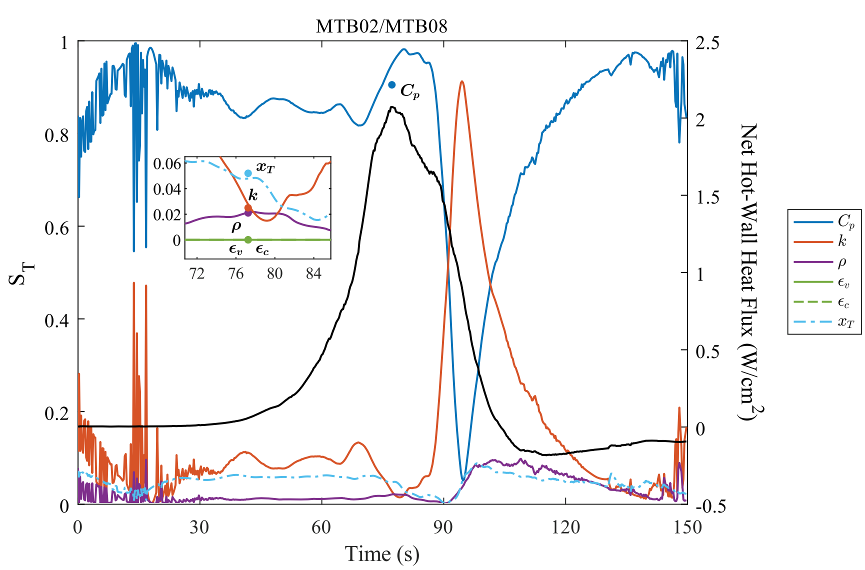

Fig. 17 Total Sobol indices for the reconstructed net hot-wall heat flux for the MTB02/MTB08 sensor pair. Labeled data points represent the total Sobol indices calculated in [4]. The solid black line is the nominal solution of q_{HW} from Fig. 12b. Inset: Magnified region for the total Sobol indices at the peak heating time.

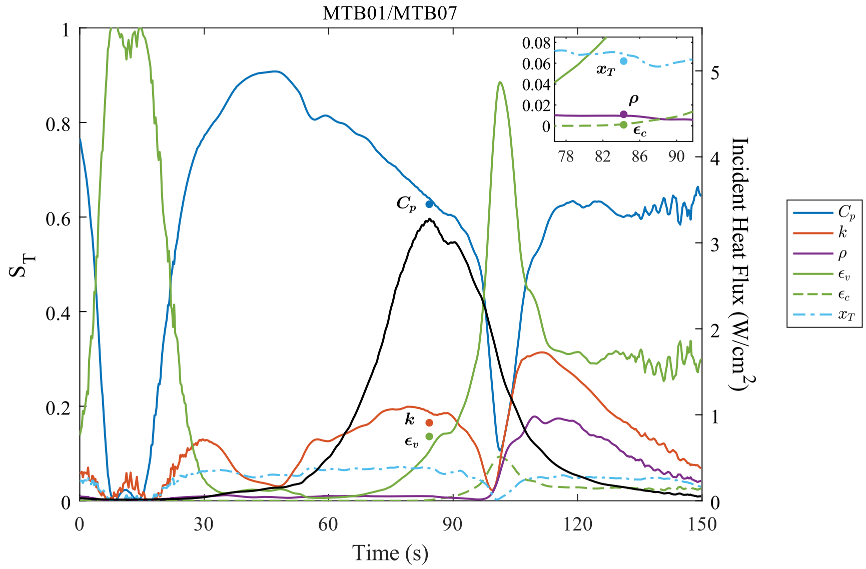

Fig. 18 Total Sobol indices for the reconstructed incident heat flux for the MTB01/MTB07 sensor pair. Labeled data points represent the total Sobol indices calculated in [4]. The solid black line is the nominal solution of q_{inc} from Fig. 12a. Inset: Magnified region for the total Sobol indices at the peak heating time.

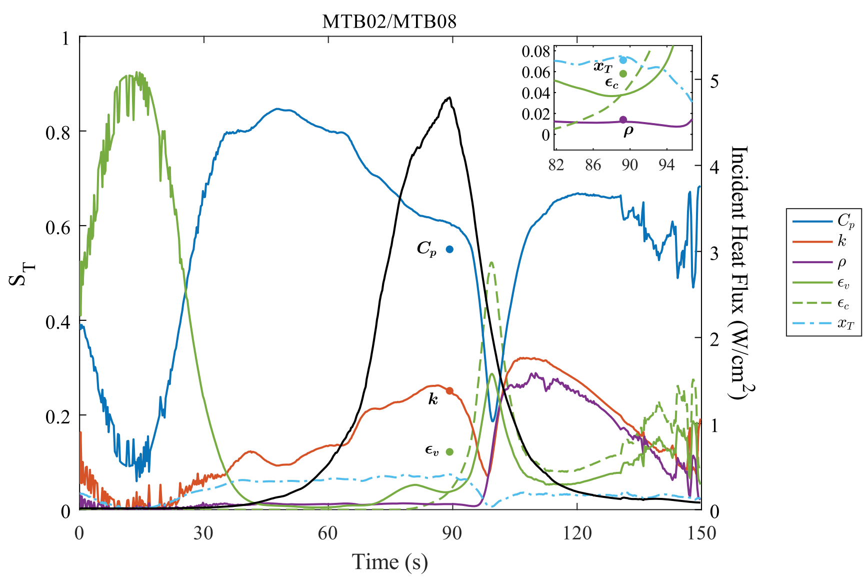

Fig. 19 Total Sobol indices for the reconstructed incident heat flux for the MTB02/MTB08 sensor pair. Labeled data points represent the total Sobol indices calculated in [4]. The solid black line is the nominal solution of q_{inc} from Fig. 12b. Inset: Magnified region for the total Sobol indices at the peak heating time.

sensor pairs, and S_{T,C_p} falls sharply, remaining low well into the cooling phase of the heat pulse.

The strong dependence of the net hot-wall heat flux uncertainty on the uncertainty of specific heat can be explained by considering how specific heat, or thermal mass ($\rho_s C_p$), dominates the transient response characteristics of the TPS thermal history near the embedded temperature probe [Eq. (1)]. The effect of thermal mass is to impart a delay into the temperature response when the TPS is subject to transient surface heating conditions. Up to peak heating, the heat flux boundary condition is increasing rapidly, such that any variation in the delay introduced in the reconstruction relative to the mean solution will induce the most significant variation in the model output. The large subsequent increase in $S_{T,k}$ following the peak heating region may be explained by considering heat soak within the TPS. Due to the highly insulating properties of the Mars 2020 backshell TPS, the short entry heat pulse likely achieved a very shallow thermal penetration depth, leading to significant thermal energy storage near the surface in the form of a hot layer. After the regime of maximum heating, the rate of heat dissipation from the near-surface hot region into the inner TPS will occur proportional to the thermal conductivity, leading to a larger propagation of thermal conductivity uncertainty into the total output uncertainty. For both sensor pairs, as the hot layer cools, the reconstruction uncertainty becomes less sensitive to variations in thermal conductivity, leading to a steady decay of $S_{T,k}$ with time.

For both sensor pairs, the uncertainty of q_{inc} (Figs. 18 and 19) up to peak heating is dominated by the uncertainty in specific heat, albeit to a lesser extent than the reconstructed net hot-wall heat flux. Generally, at the peak incident heat flux, $S_{T,C_p} \approx 0.6$ and $S_{T,k} \approx 0.2$, both of which are in good agreement with results from the prior machine learning approach. Other total Sobol indices at the peak incident heating time are also in good agreement with the prior approach, with the exception of S_{T,ϵ_v} for the MTB02/MTB08 sensor pair (Fig. 19). Immediately following the peak incident heating region, S_{T,C_p} and $S_{T,k}$ drop rapidly, and S_{T,ϵ_v} and S_{T,ϵ_c} rise. For the MTB01/MTB07 sensor pair, the virgin emissivity uncertainty begins to dominate the total output uncertainty, with $S_{T,\epsilon_v} = 0.9$ at $t = 100$ s. For the MTB02/MTB08 sensor pair, the char emissivity uncertainty begins to dominate the total output uncertainty, with $S_{T,\epsilon_c} = 0.5$ at $t = 100$ s. Following their respective peaks, S_{T,ϵ_v} and S_{T,ϵ_c} decay quickly, and S_{T,C_p}, $S_{T,k}$, and $S_{T,\rho}$ increase.

The incident heating results (Figs. 18 and 19) show a similar trend as the net hot-wall heating results (Figs. 16 and 17), where the uncertainty in heat capacity is the main driver of the reconstruction uncertainty up to peak heating. For q_{inc}, the larger value of $S_{T,k}$ up to peak heating is attributed to the effects of radiative emission at the TPS surface: while the transient thermal response characteristics of the TPS may be more strongly coupled with its thermal mass, the magnitude of the temperature rise at the surface, which contributes to radiative emission by $\tilde{T}_s^4$, is more strongly dominated by its thermal conductivity. Thus, the variation in q_{inc} becomes sensitive to the variation in the thermal conductivity. Following peak heating, the corresponding spike in either S_{T,ϵ_v} or S_{T,ϵ_c} at $t = 100$ s (Figs. 18 and 19) is attributed to the estimated char state at the TPS surface: due to the increased heating at the MTB02/MTB08 sensor pair location, the surface of the MTB02 TC plug at $t = 100$ s is estimated to be closer to a fully charred state, whereas the MTB01 TC plug surface is estimated to be only slightly pyrolyzed, resulting in different sensitivity to variation in virgin and char properties. After $t = 100$ s, the increase of $S_{T,\rho}$ can be directly attributed to how decomposition of the TPS is coupled with other model system input parameters: during pyrolysis, all thermophysical properties change as a function of the char volume fraction χ, which is itself purely a function of the solid density ρ_s relative to the densities of the fully virgin and charred states, ρ_v and ρ_c, respectively. Thus, if ρ_v and ρ_c are varied, all effective thermophysical properties during decomposition of the TPS become varied as a direct consequence, changing the output solution.

For the Mars 2020 backshell TPS, reductions in the uncertainty of specific heat and thermal conductivity will yield the most effective reduction in the reconstructed aeroheating uncertainty in the region of peak heating. Further reductions in the uncertainty of the reconstructed heating conditions following the region of peak heating can be gained by reducing the uncertainty of emissivity and density. These results highlight how the uncertainty margins attributed to postflight aerothermal environment reconstructions are dynamically sensitive to variations in the different input parameters throughout the entry heat pulse. While the peak heating total Sobol indices expose the input parameters that drive the uncertainty of the aeroheating reconstruction within the region of highest heat flux and largest reconstruction uncertainty, they are not necessarily applicable to other regions that are also considered in the design and sizing of TPS. This is a significant consideration when adapting uncertainty quantification efforts to other missions, such as Dragonfly, which utilizes a similar TPS architecture to Mars 2020 but features a prolonged convective cooling phase during atmospheric entry [40].

V. Conclusions

A Green's function-based inverse heat transfer algorithm demonstrated accurate and efficient computation of the surface heating conditions on spacecraft during atmospheric entry. The approach leverages a novel multiparameter Cole–Hopf transformation to render the governing heat conduction equation for porous, pyrolyzing solids compatible with the linear Green's function formalism. Owed to the inherent efficiency of the Green's function approach, the algorithm can recover the surface heating conditions on ablative TPS in over two orders of magnitude less time versus current state-of-the-art IHT methods, such as FIAT_Opt, all without significant sacrifices in reconstruction accuracy. The capabilities of the approach enabled a full-flight variance-based sensitivity analysis of the reconstructed heating conditions on the Mars 2020 backshell during atmospheric entry, highlighting, for the first time, how the uncertainties of specific heat, thermal conductivity, and emissivity of the Mars 2020 flight lot TPS were dominant drivers of the total reconstruction uncertainty at different times during the entry heat pulse.

These results showcase the capabilities of the Green's function approach for modeling the material response of ablative thermal protection systems and establish Green's function-based IHT methods as promising techniques for the postflight reconstruction and analysis of atmospheric entry aeroheating. The analytical and numerical techniques highlighted in this work are amenable to modeling other nonlinear material response phenomena, such as phase change, gas–surface interactions, and recession, and can be coupled with other computational tools, such as FIAT, to increase physical fidelity. Overall, access to more efficient reconstruction techniques will help reduce sizing margins, improve material models, and guide TPS characterization efforts with a substantially reduced cost.

Appendix A: Solid Decomposition

Decomposition of the TPS solid is modeled using the formulation developed for the Charring Material Thermal Response and Ablation (CMA) code [22], which is also implemented in FIAT [10]. The density of the solid phase of the TPS is modeled as a multi-component composite mixture:

$$\rho_s = (1-\phi)[\Gamma_v(\rho_A+\rho_B) + (1-\Gamma_v)\rho_C] \tag{A1}$$

where ρ_A and ρ_B are the densities of the resin constituents, and ρ_C is the density of the solid matrix. The quantity Γ_v defines the resin volume fraction in the virgin composite material. The decomposition of component i is modeled using a modified Arrhenius rate equation [10]:

$$\frac{\mathrm{d}\rho_i}{\mathrm{d}t} = -\bar{A}_i\rho_{0,i}\exp\left(-\frac{E_{A,i}}{R\tilde{T}}\right)\left[\frac{\rho_i-\rho_{r,i}}{\rho_{0,i}}\right]^{\psi_i} \tag{A2}$$

In Eq. (A2), $\bar{A}$ is a pre-exponential factor, and ρ_0 and ρ_r are the initial density and residual density of component i, respectively. In the exponential term, E_A is the activation energy for the decomposition of component i, and R is the universal gas constant. The final bracketed term is raised to the power ψ_i, specific to each constituent. The parameters in Eq. (A2) are typically determined empirically via thermogravimetric analysis [41].

Appendix B: Multiparameter Cole–Hopf Transformation

While the form of the multiparameter Cole–Hopf transform in Eq. (13) is general, the parameter β must be defined locally and for each temperature time history separately. For tractability, the effective char mass fraction χ_m is used in place of the char volume fraction χ in Eq. (13), defined as

$$\chi_m = \frac{\rho_c}{\rho_v-\rho_c}\left(\frac{\rho_v}{\rho_s}-1\right) \tag{B1}$$

The effective char mass and volume fraction are related via

$$\chi_m = \frac{\rho_c}{\rho_s}\chi \tag{B2}$$

Substituting Eq. (B2) into Eq. (13) and differentiating both sides with respect to θ yields

$$A = \left\{(1+\beta\chi_m)k(\tilde{T},0) + \beta\frac{\partial\chi_m}{\partial T}\int_0^T[k_0+k_T(T',0)]\,\mathrm{d}T'\right\}\frac{\partial T}{\partial\theta} \tag{B3}$$

In Eq. (B3), the term in curly braces is defined as $\bar{k}$, yielding

$$\bar{k}\frac{\partial T}{\partial \theta} = A \tag{B4}$$

Therefore, the condition established by Eq. (11) is best satisfied when β is defined such that

$$\frac{\bar{k}}{k} \approx 1 \tag{B5}$$

Substituting Eq. (12) into Eq. (B5) and rearranging gives

$$\left\{\frac{\chi_m k(\tilde{T},0) + \dfrac{\partial \chi_m}{\partial T}\displaystyle\int_0^T [k_0 + k_T(T',0)]\,\mathrm{d}T'}{k(\tilde{T},\chi) - k(\tilde{T},0)}\right\}\beta \approx 1 \tag{B6}$$

The term in curly braces consists of quantities that can be estimated from a single input temperature time series. As such, β is evaluated via least squares to best approximate the linear system

$$\mathbf{X}_{\boldsymbol{\beta}}\beta = \mathbf{1} \tag{B7}$$

where $\mathbf{X}_{\boldsymbol{\beta}}$ is an $N_t \times 1$ vector that represents the bracketed terms in Eq. (B6). The time series $\mathbf{X}_{\boldsymbol{\beta}}$ requires the local solution of T, ρ_s, and $\partial\chi_m/\partial T$. For a given temperature time history, $\partial\chi_m/\partial T$ can be calculated directly as follows: differentiating Eq. (B1) with respect to T yields

$$\frac{\partial \chi_m}{\partial T} = -\frac{\rho_c}{\rho_v - \rho_c}\frac{\rho_v}{\rho_s^2}\frac{\partial \rho_s}{\partial T} \tag{B8}$$

where, from Eqs. (A1) and (A2),

$$\frac{\partial \rho_s}{\partial T} = (1-\phi)\left[\Gamma_v\left(\frac{\partial \rho_A}{\partial T} + \frac{\partial \rho_B}{\partial T}\right) + (1-\Gamma_v)\frac{\partial \rho_C}{\partial T}\right] \tag{B9}$$

and

$$\begin{aligned}\frac{\partial}{\partial T}\left(\frac{\partial \rho_i}{\partial t}\right) &= -\bar{A}_i\rho_{0,i}\exp\left(-\frac{E_{A,i}}{R\tilde{T}}\right)\left[\frac{\rho_i - \rho_{r,i}}{\rho_{0,i}}\right]^{\psi_i} \\ &\quad \times \left\{\frac{E_{A,i}}{R\tilde{T}^2} + \frac{\psi_i}{\rho_{0,i}}\left[\frac{\rho_i - \rho_{r,i}}{\rho_{0,i}}\right]^{-1}\frac{\partial \rho_i}{\partial T}\right\}\end{aligned} \tag{B10}$$

Collecting the terms outside of the curly braces on the right-hand side of Eq. (B10) as $\partial\rho_i/\partial t$ and rearranging the differential terms on the left-hand side gives

$$\frac{\partial}{\partial t}\left(\frac{\partial \rho_i}{\partial T}\right) = \frac{\partial \rho_i}{\partial t}\left\{\frac{E_{A,i}}{R\tilde{T}^2} + \frac{\psi_i}{\rho_{0,i}}\left[\frac{\rho_i - \rho_{r,i}}{\rho_{0,i}}\right]^{-1}\frac{\partial \rho_i}{\partial T}\right\} \tag{B11}$$

Equation (B11) is solved forward in time to yield the time series of $\partial\rho_s/\partial T$ and $\partial\chi_m/\partial T$.

Acknowledgments

This work is supported by NASA Space Technology Graduate Research Opportunity grant 80NSSC23K1201. We acknowledge many fruitful conversations with Prof. Peter Sunderland and Todd White on the subject of this work, and we thank Georgios Bellas Chatzigeorgis, Joseph Schulz, and Sam Preece for their thorough reviews and comments.

Data Availability Statement

The Green's function-based reconstruction algorithm developed in this work, now formally called the Green's function reconstruction algorithm for inverse entry environment determination (gFRED), is available at https://github.com/kenny-mcafee/gFRED, distributed under an open-source license.

References

[1] White, T. R., Mahzari, M., Miller, R. A., Tang, C. Y., Karlgaard, C. D., Alpert, H., Wright, H. S., and Kuhl, C., "Mars Entry Instrumentation Flight Data and Mars 2020 Entry Environments," *AIAA SCITECH 2022 Forum*, AIAA Paper 2022-0011, 2022. https://doi.org/10.2514/6.2022-0011

[2] Swanson, G., Kazemba, C., Miller, R. A., Alpert, H., Williams, J., Stephen, H., and Cheatwood, N., "Overview and Performance of the LOFTID Instrumentation Suite," *AIAA SCITECH 2024 Forum*, AIAA Paper 2024-1712, 2024. https://doi.org/10.2514/6.2024-1712

[3] Gülhan, A., Thiele, T., Siebe, F., Kronen, R., and Schleutker, T., "Aerothermal Measurements from the ExoMars Schiaparelli Capsule Entry," *Journal of Spacecraft and Rockets*, Vol. 56, No. 1, 2019, pp. 68–81. https://doi.org/10.2514/1.A34228

[4] Alpert, H. S., Saunders, D. A., Mahzari, M., Monk, J. D., White, T. R., and West, T. K., "Inverse Estimation and Sensitivity Analysis of Mars 2020 Entry Aeroheating Environments," *Journal of Spacecraft and Rockets*, Vol. 60, No. 3, 2023, pp. 899–911. https://doi.org/10.2514/1.A35571

[5] Oliver, B., and Amar, A. J., "Inverse Heat Conduction Methods in the CHAR Code for Aerothermal Flight Data Reconstruction," *46th AIAA Thermophysics Conference*, AIAA Paper 2016-3384, 2016. https://doi.org/10.2514/6.2016-3384

[6] Miller, R. A., Tang, C. Y., Santos, J. A. B., White, T. R., and Cruden, B. A., "Aftbody Heat Flux Measurements During Mars 2020 Entry," *Journal of Spacecraft and Rockets*, Vol. 61, No. 2, 2024, pp. 369–382. https://doi.org/10.2514/1.A35783

[7] Mahzari, M., Braun, R. D., and White, T. R., "Reconstruction of Mars Pathfinder Aeroheating and Heat Shield Response Using Inverse Methods," *Journal of Spacecraft and Rockets*, Vol. 50, No. 6, 2013, pp. 1171–1182. https://doi.org/10.2514/1.A32462

[8] Palmer, G. E., Prabhu, D. K., Rodrigues, J., Driver, D. M., and Balboni, J. A., "CFD Simulations of Arcjet Experiments—A Survey of Recommended Practices and Lessons Learned," *AIAA AVIATION Forum and ASCEND*, AIAA Paper 2025-3480, 2025. https://doi.org/10.2514/6.2025-3480

[9] Oliver, A. B., "Development of Inverse Methods for Reconstruction of Flight Environments on Ablators," Ph.D. Thesis, Purdue Univ., West Lafayette, IN, 2016.

[10] Chen, Y.-K., and Milos, F. S., "Ablation and Thermal Response Program for Spacecraft Heatshield Analysis," *Journal of Spacecraft and Rockets*, Vol. 36, No. 3, 1999, pp. 475–483. https://doi.org/10.2514/2.3469

[11] Amar, A. J., Oliver, B., Kirk, B., Salazar, G., and Droba, J., "Overview of the CHarring Ablator Response (CHAR) Code," *46th AIAA Thermophysics Conference*, AIAA Paper 2016-3385, 2016. https://doi.org/10.2514/6.2016-3385

[12] Beck, J. V., Blackwell, B., and Haji-Sheikh, A., "Comparison of Some Inverse Heat Conduction Methods Using Experimental Data," *International Journal of Heat and Mass Transfer*, Vol. 39, No. 17, 1996, pp. 3649–3657. https://doi.org/10.1016/0017-9310(96)00034-8

[13] Mahzari, M., "Inverse Estimation Methodology for the Analysis of Aeroheating and Thermal Protection System Data," Ph.D. Thesis, Georgia Inst. of Technology, Atlanta, GA, 2013.

[14] Mahzari, M., Braun, R. D., White, T. R., and Bose, D., "Inverse Estimation of the Mars Science Laboratory Entry Aeroheating and Heatshield Response," *Journal of Spacecraft and Rockets*, Vol. 52, No. 4, 2015, pp. 1203–1216. https://doi.org/10.2514/1.A33053

[15] Beck, J. V., "Nonlinear Estimation Applied to the Nonlinear Inverse Heat Conduction Problem," *International Journal of Heat and Mass Transfer*, Vol. 13, No. 4, 1970, pp. 703–716. https://doi.org/10.1016/0017-9310(70)90044-X

[16] Osman, A. M., and Beck, J. V., "Nonlinear Inverse Problem for the Estimation of Time-and-Space-Dependent Heat-Transfer Coefficients," *Journal of Thermophysics and Heat Transfer*, Vol. 3, No. 2, 1989, pp. 146–152. https://doi.org/10.2514/3.141

[17] Cai, Z., Liu, T., Wang, B., Rubal, J., and Sullivan, J. P., "Numerical Inverse Heat Transfer Analysis for Temperature-Sensitive-Paint Measurements in Hypersonic Tunnels," *Journal of Thermophysics and Heat Transfer*, Vol. 25, No. 1, 2011, pp. 59–67. https://doi.org/10.2514/1.49217

[18] Cole, K., Beck, J., Haji-Sheikh, A., and Litkouhi, B., *Heat Conduction Using Greens Functions*, 2nd ed., CRC Press, Boca Raton, FL, 2010.

[19] Nguyen, N. M., Ruda, M. L., and Massa, L., "Effect of Insulations and Coatings on Hypersonic Heat Flux Reconstruction," *Journal of Thermophysics and Heat Transfer*, Vol. 35, No. 1, 2021, pp. 63–79. https://doi.org/10.2514/1.T5995

[20] Whalen, T. J., Laurence, S. J., Marineau, E. C., and Ozawa, H., "A Green's Function Approach to Heat-Flux Estimation from Temperature-Sensitive Paint Measurements," *Measurement Science and Technology*, Vol. 32, No. 11, 2021, Paper 114011. https://doi.org/10.1088/1361-6501/ac16ee

[21] Massa, L., and Schetz, J. A., "Hypersonic Heat Flux Reconstruction with Distributed Temperature Sensors," *Journal of Thermophysics and Heat Transfer*, Vol. 34, No. 2, 2020, pp. 331–346. https://doi.org/10.2514/1.T5778

[22] Moyer, C., and Rindal, R., "An Analysis of the Coupled Chemically Reacting Boundary Layer and Charring Ablator: Part 2," NASA CR 1061, 1968.

[23] Bessire, B. K., Meurisse, J. B., Panerai, F., and Mansour, N., "Material Response Analysis of PICA-NuSil at the Hypersonic Materials Environmental Test System," *AIAA AVIATION 2023 Forum*, AIAA Paper 2023-3325, 2023. https://doi.org/10.2514/6.2023-3325

[24] Chen, Y.-K., "Thermal Analysis for Phenolic Impregnated Carbon Ablator/CV-1144-0 in Hypersonic Test Environments," *Journal of Spacecraft and Rockets*, Vol. 59, No. 2, 2022, pp. 587–599. https://doi.org/10.2514/1.A35167

[25] Vadasz, P., "Analytical Solution to Nonlinear Thermal Diffusion: Kirchhoff Versus Cole–Hopf Transformations," *Journal of Heat Transfer*, Vol. 132, No. 12, 2010, Paper 121302. https://doi.org/10.1115/1.4002325

[26] Hansen, P. C., "Deconvolution and Regularization with Toeplitz Matrices," *Numerical Algorithms*, Vol. 29, No. 4, 2002, pp. 323–378. https://doi.org/10.1023/A:1015222829062

[27] Tikhonov, A. N., and Arsenin, V. Y., *Solutions of Ill-Posed Problems*, V. H. Winston & Sons, Washington, D.C., 1977.

[28] McAfee, K., Alpert, H., Sunderland, P., and Rabin, O., "A Green's Function Sensor Fusion Approach for Evaluating Spacecraft Entry Heating from On-Board Thermal Instrumentation," *AIAA AVIATION Forum and ASCEND 2024*, AIAA Paper 2024-4033, 2024. https://doi.org/10.2514/6.2024-4033

[29] Brandis, A., Hwang, H., Gulhan, A., Santos, J., Stern, E., and Siebe, F., "Overview of the Dragonfly Entry Aerosciences Measurements (DrEAM) Suite," *18th International Planetary Probe Workshop*, Virtual, 2021.

[30] Ma, J., Rokhlin, V., and Wandzura, S., "Generalized Gaussian Quadrature Rules for Systems of Arbitrary Functions," *SIAM Journal on Numerical Analysis*, Vol. 33, No. 3, 1996, pp. 971–996. https://doi.org/10.1137/0733048

[31] Yang, T. Y., *Finite Element Structural Analysis*, Prentice-Hall, Upper Saddle River, NJ, 1986.

[32] Lachaud, J., van Eekelen, T., Bianchi, D., and Martin, A., "TACOT v3.0," *6th Ablation Workshop*, Urbana, IL, 2014.

[33] Lachaud, J., and Mansour, N. N., "Porous-Material Analysis Toolbox Based on OpenFOAM and Applications," *Journal of Thermophysics and Heat Transfer*, Vol. 28, No. 2, 2014, pp. 191–202. https://doi.org/10.2514/1.T4262

[34] Monk, J., Feldman, J. D., Mahzari, M., Santos, J. A., White, T. R., Prabhu, D. K., and Alpert, H., "MEDLI2 Material Response Model Development and Validation," *AIAA SCITECH 2022 Forum*, AIAA Paper 2022-0549, 2022. https://doi.org/10.2514/6.2022-0549

[35] Gokcen, T., and Alunni, A., "On Laminar to Turbulent Transition of Arc-Jet Flow in the NASA Ames Panel Test Facility," *43rd AIAA Thermophysics Conference*, AIAA Paper 2012-3304, 2012. https://doi.org/10.2514/6.2012-3304

[36] Mahzari, M., Beck, R., Hwang, H., Monk, J., Morgan, J., Williams, J., and Edquist, K. T., "Development and Sizing of the Mars2020 Thermal Protection System," *AIAA AVIATION 2022 Forum*, AIAA Paper 2022-3951, 2022. https://doi.org/10.2514/6.2022-3951

[37] Sobol, I. M., "Global Sensitivity Indices for Nonlinear Mathematical Models and Their Monte Carlo Estimates," *Mathematics and Computers in Simulation*, Vol. 55, No. 1, 2001, pp. 271–280. https://doi.org/10.1016/S0378-4754(00)00270-6

[38] Saltelli, A., Annoni, P., Azzini, I., Campolongo, F., Ratto, M., and Tarantola, S., "Variance Based Sensitivity Analysis of Model Output. Design and Estimator for the Total Sensitivity Index," *Computer Physics Communications*, Vol. 181, No. 2, 2010, pp. 259–270. https://doi.org/10.1016/j.cpc.2009.09.018

[39] Jansen, M. J. W., "Analysis of Variance Designs for Model Output," *Computer Physics Communications*, Vol. 117, No. 1, 1999, pp. 35–43. https://doi.org/10.1016/S0010-4655(98)00154-4

[40] Stern, E., and Mahzari, M., "Dragonfly TPS Sizing and Analysis," *AIAA SCITECH 2023 Forum*, AIAA Paper 2023-0603, 2023. https://doi.org/10.2514/6.2023-0603

[41] Laub, B., Chen, Y.-K., and Dec, J., "Development of a High-Fidelity Thermal/Ablation Response Model for SLA-561V," *41st AIAA Thermophysics Conference*, AIAA Paper 2009-4232, 2009. https://doi.org/10.2514/6.2009-4232

G. E. Palmer
Associate Editor